

Quantifying Morphological Changes & Sediment Transport Pathways on Comet 67P/Churyumov-Gerasimenko

Megan Nicole Barrington¹, Samuel Birch², Abhinav Jindal¹, Alexander G. Hayes¹, Paul Corlies³, and Jean-Baptiste Vincent⁴

¹Cornell University

²Massachusetts Institute of Technology

³Cornell University

⁴DLR Institute for Planetary Research

December 21, 2022

Abstract

Comets are active geological worlds with primitive surfaces that have been shaped to varying degrees by sublimation-driven sediment transport processes. Rosetta's rendezvous with comet 67P/Churyumov-Gerasimenko (67P) in 2014 provided data with the necessary spatial and temporal resolutions to observe how micro-gravity worlds evolve. Rosetta's observations have thus far revealed that the majority of changes to the surface occurred within 67P's smooth terrains, vast sedimentary deposits that blanket a significant fraction of the nucleus. Understanding the global context of these changes, and therefore the sediment transport pathways that govern the evolution of 67P's surface requires a thorough description of their changing morphologies, and an evaluation of existing global-scale spatial and temporal trends. Accordingly, we present a time-resolved synthesis of erosion and deposition activity on comet 67P as it passed through its August 13, 2015 perihelion from September, 2014 to August, 2016. Our mapping results indicate that, around perihelion, sediment is globally redistributed inter-regionally from 67P's more active south to the north. Equally important, however, are local, topographically-influenced sediment transport processes, with large volumes of sediment moving intra-regionally over sub-kilometer scales. We also show evidence for regions of near-zero net erosion/deposition between approximately 30–60° latitude, which may act as terminal sedimentary sinks, with remobilization of these materials hindered by multiple factors. This work provides a complete mapping of the sediment transport processes and pathways across 67P observed by the Rosetta mission, and represents a critical step toward understanding the global landscape evolution of cometary surfaces.

Hosted file

952366_0_art_file_10544739_rn1k24.docx available at <https://authorea.com/users/568283/articles/614201-quantifying-morphological-changes-sediment-transport-pathways-on-comet-67p-churyumov-gerasimenko>

Hosted file

952366_0_supp_10544744_rn1lh2.docx available at <https://authorea.com/users/568283/articles/614201-quantifying-morphological-changes-sediment-transport-pathways-on-comet-67p-churyumov-gerasimenko>

1
2 **Quantifying Morphological Changes & Sediment Transport Pathways on Comet**
3 **67P/Churyumov-Gerasimenko**

4 **M. N. Barrington¹, S. P. D. Birch^{2,3}, A. Jindal³, A. G. Hayes³, P. Corlies^{2,3†}, and J.-B.**
5 **Vincent⁴**

6 ¹ Department of Earth and Atmospheric Sciences, Cornell University, Ithaca, NY, USA

7 ²Department of Earth, Atmospheric, and Planetary Sciences, Massachusetts Institute of
8 Technology, Cambridge, MA, USA. ³Department of Astronomy, Cornell University, Ithaca, NY,
9 USA. ⁴DLR Institute of Planetary Research, Berlin, Germany.

10
11 Corresponding author: Megan Barrington (mne8@cornell.edu)

12
13 † Current address: Spectral Sciences Inc. 4 Fourth Ave., Burlington, MA, 01803

14 **Key Points:**

- 15
- Sediment is intra- and inter-regionally redistributed.
 - Erosion and deposition follow the subsolar latitude, and are strongly influenced by local topography.
 - Scarp activity is primarily limited to equatorial and internal regions.
 - We observe net zero erosion/deposition on the tops of the lobes, perhaps indicating the presence of terminal sinks for airfalling sediment.
- 16
17
18
19
20
21

22 **Abstract**

23 Comets are active geological worlds with primitive surfaces that have been shaped to varying
24 degrees by sublimation-driven sediment transport processes. Rosetta's rendezvous with comet
25 67P/Churyumov-Gerasimenko (67P) in 2014 provided data with the necessary spatial and
26 temporal resolutions to observe how micro-gravity worlds evolve. Rosetta's observations have
27 thus far revealed that the majority of changes to the surface occurred within 67P's smooth
28 terrains, vast sedimentary deposits that blanket a significant fraction of the nucleus.
29 Understanding the global context of these changes, and therefore the sediment transport
30 pathways that govern the evolution of 67P's surface requires a thorough description of their
31 changing morphologies, and an evaluation of existing global-scale spatial and temporal trends.
32 Accordingly, we present a time-resolved synthesis of erosion and deposition activity on comet
33 67P as it passed through its August 13, 2015 perihelion from September, 2014 to August, 2016.
34 Our mapping results indicate that, around perihelion, sediment is globally redistributed inter-
35 regionally from 67P's more active south to the north. Equally important, however, are local,
36 topographically-influenced sediment transport processes, with large volumes of sediment moving
37 intra-regionally over sub-kilometer scales. We also show evidence for regions of near-zero net
38 erosion/deposition between approximately 30–60° latitude, which may act as terminal
39 sedimentary sinks, with remobilization of these materials hindered by multiple factors. This work
40 provides a complete mapping of the sediment transport processes and pathways across 67P
41 observed by the Rosetta mission, and represents a critical step toward understanding the global
42 landscape evolution of cometary surfaces.

43

44 **Plain Language Summary**

45 Comets are some of the oldest materials in the solar system. When these ice-rich bodies
46 approach the sun, the ices at the surface change phase from solid to gaseous. The change in
47 phase of ices at the surface is the primary cause for the breaking of solid materials into smaller
48 bits, as well as the movement of material around and off of the comet's surface. On comet 67P,
49 where boulders, rocks, gravels and finer materials coat most of the northern surface, this phase
50 change can move material in many different ways. Determining how and where materials are
51 moving across the entire comet can help understand how the ice content of the comet may have
52 changed since it formed. Using our observations of the changing geology of 67P, we can make
53 predictions about geologic processes acting on other comet surfaces.

54

55 **1 Introduction**

56 Comets are composed of primitive materials that once existed frozen in the outer realm of
57 the solar system. These remnants of the earliest era of planetary formation were eventually
58 transported to their current reservoirs through planetary migration and/or interactions with other
59 stars and gas clouds (A'Hearn, 2012). Jupiter Family Comets (JFCs) are of particular interest for
60 scientific study due to their short orbital periods, and close perihelion passages that permit
61 detailed spacecraft observations. Broadly, as these objects migrated increasingly closer to the
62 Sun, their volatile-rich surfaces began to evolve as various ices exposed at the surface
63 sublimated. This process drives the physical and chemical weathering of the consolidated

64 nucleus, wherein sediment is produced and transported either across, or entirely ejected from, the
65 surface.

66 Of the five JFCs visited by spacecraft observations to date, four have been sufficiently
67 resolved to permit geological studies of their surfaces. These include 81P/Wild 2 (Brownlee et
68 al., 2004), 9P/Tempel 1 (Thomas et al., 2013a; Veverka et al., 2013), 103P/Hartley 2 (Thomas et
69 al., 2013b), and 67P/Churyumov-Gerasimenko (67P) (El-Maarry et al., 2017). These
70 observations all showed that cometary nuclei are complex worlds, with regions of
71 unconsolidated sedimentary grains coating an otherwise consolidated, rugged nucleus (Sunshine,
72 2016). Meanwhile observations of comets 19P/Borrelly (Soderblom et al., 2002) and 1P/Halley
73 (Reinhard, 1986), though hinting at similar landscapes, had insufficient resolutions for more
74 quantitative analyses.

75 Of these five JFCs, the highest spatial and temporal resolution datasets documented
76 comet 67P. Rosetta collected over 8,200 high resolution images of 67P's surface over the span of
77 the mission's two year visit to the comet from 2014 to 2016 (Keller, 2007). These data provide a
78 unique opportunity to observe high spatial and temporal resolution changes occurring on 67P's
79 smooth terrains. Here, the term smooth terrains is used as a catch-all term to describe
80 morphologies which have previously been described as smooth terrains, cauliflower plains, and
81 pitted plains on comet 67P (Birch et al., 2017; Moruzzi et al., 2022). Smooth terrains are
82 composed of sedimentary grains that are likely sourced from the consolidated nucleus, albeit by
83 unknown means. Sublimation of ice within the consolidated nucleus then weathers the nucleus,
84 accelerating liberated particles off the surface. Larger grains then follow ballistic trajectories and
85 fall back to the surface, depositing as 'airfall' in topographical and gravitational lows in the
86 comet's northern latitudes (Fig. 1; Keller, 2017). Airfall grain sizes range from centimeter to
87 decimeter scale (Keller, 2017), and are heterogeneous in both their size distribution (Pajola,
88 2017) and volatile content (Davidsson et al., 2021) across the surface of 67P. While it was
89 initially hypothesized that these airfall materials would act as an insulating layer that would
90 suppress activity from the more ice-rich layers below (Keller, 1986), Rosetta instead observed
91 that the smooth terrains hosted the majority of large-scale changes. This suggests that the
92 sedimentary grains retain large volumes of volatile ices despite their exposure within the coma
93 during transport. Indeed, Davidsson et al. (2021) found that for a transit time of 12 hours,
94 centimeter sized particles retained ~50% of their original water ice, with decimeter sized
95 particles retaining up to ~90%. More volatile ices (e.g., CO, CO₂), however, are depleted well
96 within typical transit times unless buried within the cores of larger grains.

97 Past work has documented several types of morphological units on 67P, including
98 consolidated nucleus materials (a.k.a consolidated terrain), which often outcrop in the form of
99 cliffs within smooth terrain regions, as well as bouldered terrains, talus deposits, smooth terrains,
100 cauliflower plains, and pitted plains (Birch et al., 2017). Surface changes that have been
101 examined in detail include depressions (Birch et al., 2017), scarps (Birch et al., 2017, El-Maarry,
102 2017; Jindal et al., 2022), honeycomb features (Shi et al., 2016; Hu et al., 2017; El-Maarry et al.,
103 2019), ripples (El-Maarry et al., 2017; Jia et al., 2017), pits (Deshapriya et al., 2016), and bright
104 spots (Deshapriya et al., 2016; Fornasier et al., 2016). Although these many studies documented
105 the evolution of isolated regions and features on 67P, a synthesis of the evolution of all of 67P's
106 smooth terrains has remained unexplored. Thus, it is necessary to study the global geologic
107 processes which have acted on 67P, a task that will have broad implications for cometary
108 surfaces more generally as smooth terrains appear ubiquitous across all of the cometary nuclei
109 imaged with sufficient resolution to identify them. Herein, we present a synthesis of the

110 sublimation-driven surface evolution and sediment re-distribution of the smooth terrains of
111 comet 67P.
112

113 **2 Methods**

114 We utilized images collected by Rosetta's Optical, Spectroscopic, and Infrared Remote
115 Sensing Imaging System (OSIRIS) Near Angle Camera (NAC), which acquired over 8,200
116 images of the surface of comet 67P. These data document both the coma and the surface of the
117 comet before, during, and after 67P's 2015 perihelion passage. Previous mapping of 67P (El-
118 Maarry et al., 2015; Thomas et al., 2015) documented smooth terrain deposits across the comet,
119 with most deposits found in 67P's northern hemisphere (Birch et al., 2017; El-Maarry et al.,
120 2015). For portions of the comet containing known smooth terrains, we divided them into 25
121 distinct sub-regions, with naming conventions based on the nomenclature from El-Maarry et al.
122 (2015) (Fig. 1). This subdivision was done out of necessity because of (1) the comet's complex
123 geometry, (2) data quality variations, (3) data coverage gaps, and (4) the vast latitudinal and
124 longitudinal expanse of several previously defined (El-Maarry et al., 2015) regions. Despite
125 various attempts to generate an automated image processing pipeline, we determined that manual
126 image selection was the most efficient way to find images that: (1) met resolution requirements,
127 (2) displayed a significant portion of a given region under investigation, (3) did not display
128 locally saturated data, and (4) provided optimal viewing geometry and phase angles for detection
129 of 1–10 meter scale changes. To reduce errors in change detection due to variations in viewing
130 geometry, phase angles between 45–90° were preferentially selected for image analysis, with
131 >90% of images falling within this range (Table S1). Due to inconsistent coverage of each
132 region, more extreme phase angles were also utilized as necessary when higher quality
133 observations were not available (Table S1).

134 Our method of manual image selection, projection, and change detection was performed
135 in multiple steps. First, reference images were manually selected for each sub-region as early as
136 data coverage of each region allowed. Next, follow-up images of each sub-region were selected,
137 initially at a cadence of once per month after the date of their respective reference images. If
138 changes were detected between two consecutive images at this cadence, the image cadence was
139 increased systematically until either no further changes were detected between consecutive
140 images, or until coverage of the region was not available at a shorter interval of time. Whenever
141 possible, we leverage multiple images of a given surface change, though sporadic coverage and
142 changing resolution/imaging conditions meant such confirmations, as well as precise
143 determinations about the dates on which changes began/ceased were not always possible (yellow
144 boxes in Table S3).

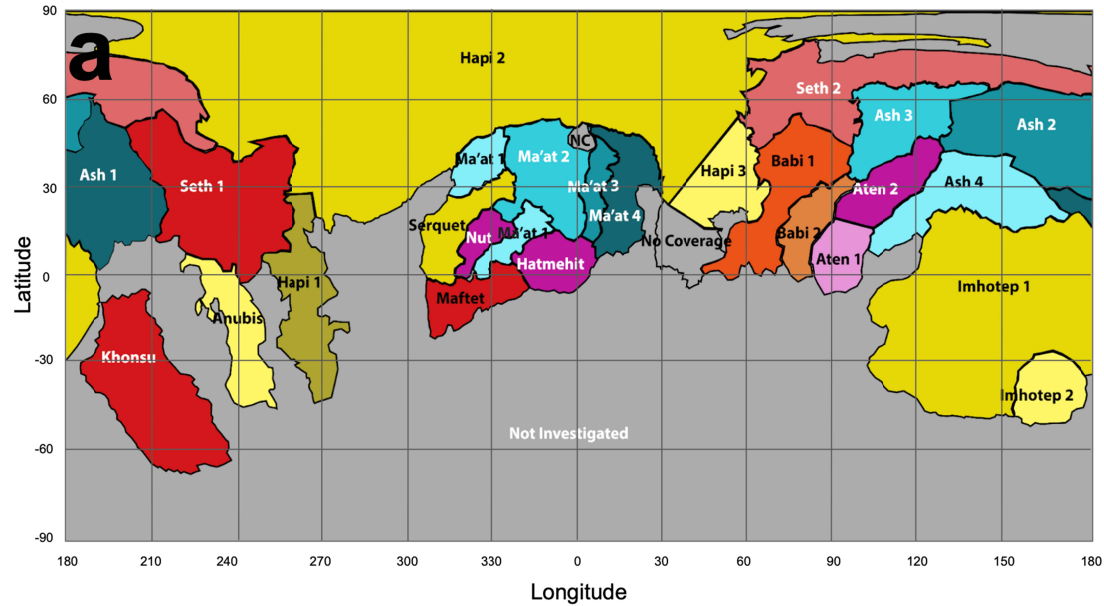
145 For each sub-region, we then projected each image into the frame of our reference image
146 using the ShapeViewer (www.comet-toolbox.com) software package (Vincent 2018). This
147 allowed us to blink images and more reliably detect finer-scale changes and their precise
148 locations than what would otherwise be possible by analyzing unprojected images side-by-side.
149 ShapeViewer also allowed for viewing high-resolution, small field-of-view images in a global
150 context, aiding in our later interpretations. Finally, for each region, mapping of all changes was
151 performed in the ArcGIS software as shapefiles and layers. Identified changes, each confirmed
152 by at least two individual mappers, were annotated and analyzed for 619 images in total (Table
153 S1) with resolutions ranging from approximately 0.1–20 m/pixel. If necessary, the contrast and
154 brightness of each image was adjusted to provide better perspective for the interpretation of

155 possible changes in each image. Measurements of distance and feature size were made in
156 ArcMap by converting an arbitrary unit to meters using scale bars created during layer
157 generation in Shapeviewer.

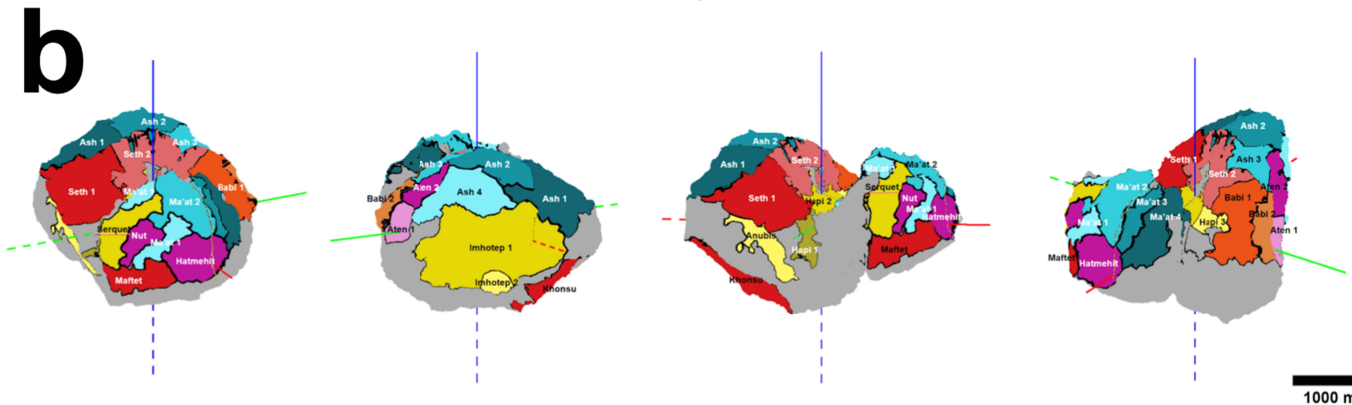
158 It is important to note that data coverage was incomplete, especially near perihelion from
159 mid- to late-2015 as the Rosetta spacecraft backed away from the comet. This resulted in images
160 having far coarser resolution during these most active periods. Images also had variable phase
161 angles and illumination conditions, further complicating our search for changes. For example,
162 data over 67P's northern latitudes were progressively more difficult to use, eventually becoming
163 unusable when those latitudes entered polar winter (black boxes in Table S3). Resolution
164 limitations were addressed first by including estimated uncertainties (yellow boxes, Table S3)
165 between dates when changes were observed and the earliest date a change may have occurred
166 before our observation. Next, wherever possible, observations were confirmed in sequential
167 images. Whenever a candidate change was unclear due to poor resolution, the changes were
168 flagged as 'low-confidence' observations (Table S2), and were not included in the synthesis of
169 activity in the northern hemisphere. Sequential images whose average phase angles vary by
170 greater than 45° were also flagged in Table S1. Therefore, while we know our mapping is
171 incomplete near perihelion and for scales below ~ 1 meter, our consistent image selection,
172 projection, and stretching routine allowed us to place constraints on when we were certain
173 activity occurred in a given region (green boxes in Table S3) and when it was possible, but not
174 confirmed that activity occurred (yellow boxes in Table S3). We accordingly specify that
175 observations occur by a specific date to indicate the latest possible date on which a change
176 occurred, as limited by either resolution, shadows, viewing geometry, or data coverage.

177 We identified and searched for six types of changes in each of our 25 sub-regions. These
178 changes included boulder burial, boulder exposure, boulder migration, scarp migration (Fig. 2),
179 plains migration (Fig. 3), and honeycomb evolution (Fig. 4). See Table S2 for a complete catalog
180 of detected changes. For the purposes of our work, boulder burial includes only boulders that
181 were totally covered by the deposition of new smooth terrains (Fig. 2), as varying illumination
182 conditions and distortions inherent to the projection of images complicated our ability to
183 interpret any partial burials. Boulder exposure likewise describe boulders which had been
184 completely covered by smooth terrains and were later revealed, but does not include already
185 exposed boulders undergoing further local erosion for the same reasons as above (Fig. 2).
186 Exposures and burials of outcrops of the underlying consolidated nucleus were interpreted
187 similarly to their boulder counterparts and were classified in these same categories for simplicity.
188 Boulder migration documents the movement of boulders ranging from meters to tens of meters in
189 diameter within talus deposits and boulder fields, falling from local cliffs, or those being
190 emplaced from regions beyond individual image boundaries (i.e., the initial boulder location is
191 not known). Differentiation between boulder exposures and boulder migrations were typically
192 made based on two factors: 1) Previous indication(s) of a boulder's presence. Visible evidence of
193 boulders beneath the surface sediment, such as mounds of sediment where a boulder is later
194 exposed, are all classified as boulder exposures. 2) The boulder's proximity to talus deposits. If
195 the pre-existing location of a boulder cannot be determined, the boulder is classified as migration
196 when located within or proximal to a talus deposit. If distal from any talus deposit or cliff within
197 the center of a smooth terrain deposit, we instead classify as boulder exposures. One exception is
198 the ~ 10 meter scale boulder that migrated from an unknown cliff into Hapi 1 (Fig. 2),
199 distinguished by slight impact impressions near the new boulder in the center of the region.

200



201



202

203 **Figure 1. a)** An equirectangular projection of our 25 sub-regions of smooth terrains analyzed for surface evolution. Colored regions
 204 are dominated by smooth terrains, while the regions in gray show few smooth terrains, instead being dominated by consolidated
 205 materials. Gray regions were not considered in our work. Regions labeled ‘No Coverage’ and ‘NC’ were not investigated due to
 206 insufficient coverage in reference images. **b)** Four orientations of a 3D projection of 25 sub-regions of smooth terrains on 67P. X-
 207 Axis: Red, Y-Axis: Green, Z-Axis: Blue. Dashed lines represent negative axis directions.

208 Scarp migration describes the formation and/or subsequent movement of arcuate or semi-
209 arcuate depressions (Fig. 2), all of which are bounded at least on one side by a migrating scarp
210 wall. These depressions are typically observed migrating radially from a topographic
211 discontinuity, although the genesis point is not always clear (Birch et al., 2019; Jindal et al.,
212 2022). The radial migration of the scarps is key in differentiating between the processes of scarp
213 migration and plains migration.

214 Plains migration describes the re-distribution of sediment deposits which form mounds or
215 dune-like crests (Fig. 3; Thomas et al., 2019). We detected this process by analyzing the
216 movement of these mounds and crests, identifying variations in surface roughness, and/or
217 observing changing locations of the boundaries between smooth terrains and neighboring
218 consolidated regions.

219 Finally, honeycomb evolution describes the increase or decrease in surface roughness of
220 “honeycombs” (Hu et al. 2017; Shi et al., 2016; El-Maarry et al., 2019). These ten meter scale,
221 highly textured areas form just beneath some smooth terrains. As such, they experience a
222 reduction in surface roughness when new granular materials are deposited, and an increase in
223 roughness when overlying material is eroded (Fig. 4; Shi et al., 2016).

224 In addition to the six broad types of change described above, several additional isolated
225 types of changes were observed throughout the mission. These include the formation of bright,
226 likely ice-rich, pits in Khonsu (Fig. 5; Deshapriya et al., 2016; Fornasier et al., 2015; Oklay et
227 al., 2016), the destruction and subsequent reformation of a set of ripple bedforms in Hapi 1 (Fig.
228 S2; El-Maarry et al., 2017; Jia et al., 2017), and quasi-circular pits that appear in Ash 1.

229 We classified each type of change into categories of erosion, deposition, or re-distribution
230 for the synthesis of global sediment transport trends and sorted into sequential three-month time
231 bins beginning in August, 2014 and ending in August, 2016 (Table S3; Fig. 6–8). The first three
232 time bins are Pre-Perihelion 1, 2 and 3. Images from these time bins were taken before 67P’s
233 August 2015 perihelion. The next two time bins, Near-Perihelion 1 and 2, group images
234 collected a few months before, during, and a few months after perihelion. Finally, images
235 grouped into the last three time bins, Post-Perihelion 1, 2, and 3, were taken after 67P had passed
236 perihelion.

237 Each Scarp migration, boulder/nucleus exposure, boulder migration, increased surface
238 roughness in honeycombs, and pit formation in Ash and Khonsu are all classified as erosional
239 processes. All these processes act to remove granular smooth terrain material on the surface,
240 most likely driven by the sublimation of near-surface volatile ices (Hu et al., 2017; El-Maarry et
241 al., 2017; Birch et al., 2019; Jindal et al., 2022). We classify boulder burials, nucleus burials, and
242 decreased surface roughness of honeycombs as indicators of deposition of new smooth terrain
243 sediment. While other research classifies the burial of scarps as a depositional indicator (Jindal et
244 al., 2022), we did not include them here due to the difficulty of classifying fading scarps with
245 varying viewing geometries. However, we still used scarp fading/burial to better interpret trends
246 in our data when appropriate. Finally, the reformation of ripples in Hapi 1, as well as the general
247 migration of plains are classified as redistributions of sediment. We specifically classify these
248 separately because, though we know changes occurred, we cannot conclude whether erosion or
249 deposition occurred (or both) due to the lack of nearby topographic benchmarks like boulders or
250 the underlying nucleus. For example, the migration of plains materials and dune-like crests
251 clearly show movement of granular materials, but the movement could be due either to small
252 impacts splashing particles on the surface downslope (Thomas et al., 2015), or due to ice
253 sublimation in the near surface moving small volumes of materials.

254 **3 Results**

255 3.1 Pre-Perihelion Activity

256 3.1.1 Pre-Perihelion 1

257 The earliest onset of activity occurred as limited erosion within Hapi 1 during Pre-
258 Perihelion 1 (September–November, 2014). Two boulders were exposed in the center of the
259 region on September 12, 2014. We also observed the potential migration of features analogous to
260 aeolian ripples (El-Maarry et al., 2017; El-Maarry et al., 2019; Davidsson et al., 2015; Jia et al.,
261 2016) in Hapi 1 from September 2–September 12, 2014, although this initial change in position
262 may be an artifact of the image projection process. Barucci et al. (2016) first described the
263 presence of bright patches during this epoch, which they interpreted to be spectrally bright due to
264 the presence of water ice. These patches occurred as individual boulders/patches in a western
265 alcove of Imhotep 1 and in Imhotep 1’s eastern pitted region (Barucci et al., 2016), and as a
266 cluster at the boundary of Imhotep 1 and Apis (Barucci et al., 2016; Oklay et al., 2016). These
267 specific features persisted for months, although lifespans of other bright spots varied (Barucci et
268 al., 2016). We did not search for instances of bright patches in this work, as they often occurred
269 at borders between consolidated and smooth terrain regions. We detected no erosional or
270 depositional activity associated with these spectral changes.

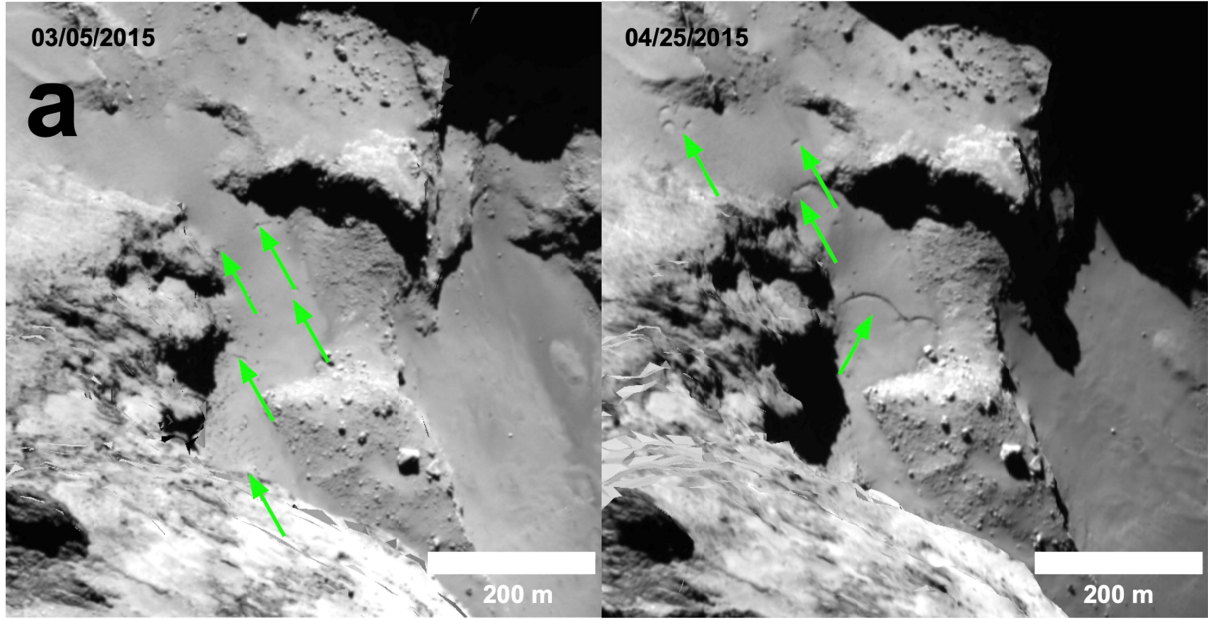
271

272 3.1.2 Pre-Perihelion 2

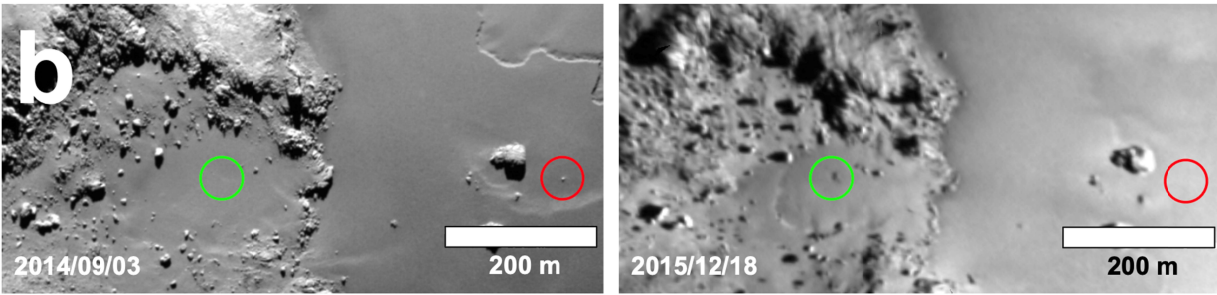
273 Erosion, deposition and re-distribution of smooth terrains began in earnest during Pre-
274 Perihelion 2, from December 2014 until February 2015 (Figure 4). We detected scarps migrating
275 within Hapi 2, Hapi 3 and Seth 2 by December, 2014 and within Seth 1 by January 23, 2014. The
276 migrating scarps within Hapi 2 are of particular interest during this epoch, as large quasi-arcuate
277 scarp fronts emanated from 67P’s north pole toward Hapi 1 and Hapi 3 between December 30,
278 2014 and February 9, 2015. While scarp migrations were recorded in the Hapi region by El-
279 Maarry et al. (2017), we show here that they began at least one month prior to their observations.
280 These scarp migrations continued through February, 2015 within Seth 1, Seth 2, Hapi 2, and
281 Hapi 3. We also observed boulder exposures in Ash 3, Hapi 3, and possibly in Hapi 2. In Ash 3,
282 two boulders were exposed by December 2, 2014. Much greater erosion appears to have
283 occurred within Hapi 2, as migrating scarps exposed five boulders on December 30, 2014, and
284 another 16 by January 22, 2015. With the exception of Ash 3, we consider all of these regions to
285 be “internal”, meaning they are all located directly within the neck, or they are near the neck
286 region and have a significant portion of their surface tilted toward the Hathor cliff. While many
287 of these regions are proximal to the neck, our observations clearly show that erosional activity
288 also expanded south of (away from) the neck.

289 Hu et al. (2017) and El-Maarry et al. (2019) described honeycombs that began to evolve
290 in Ma’at by January 22, 2015, and in the Nut and Serqet regions by February 14, 2015, including
291 depressions that would later mature into honeycombs. Our own observations indicate the large-
292 scale redistribution of smooth terrain materials within Ma’at 4 on February 21, 2015.

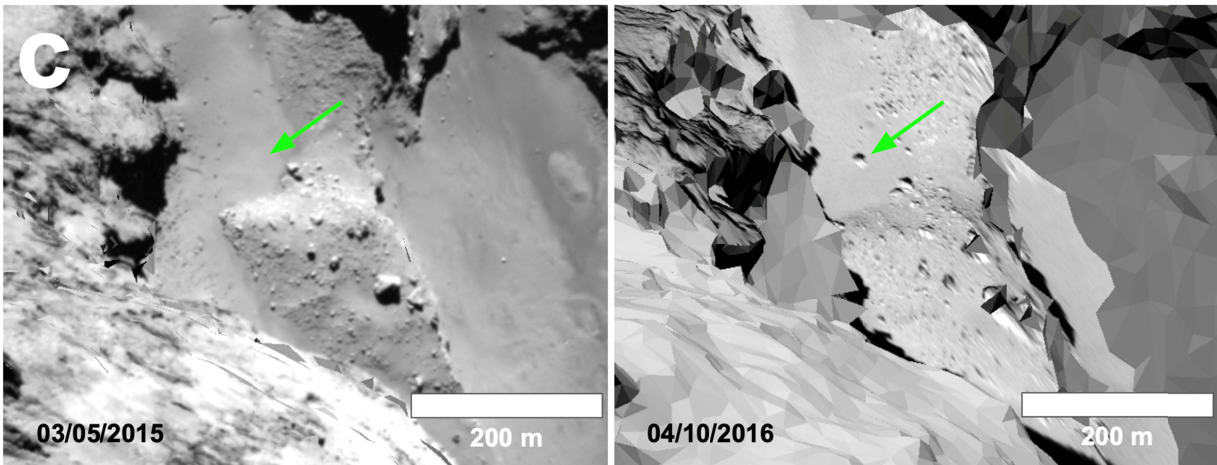
293



294



295



296

297

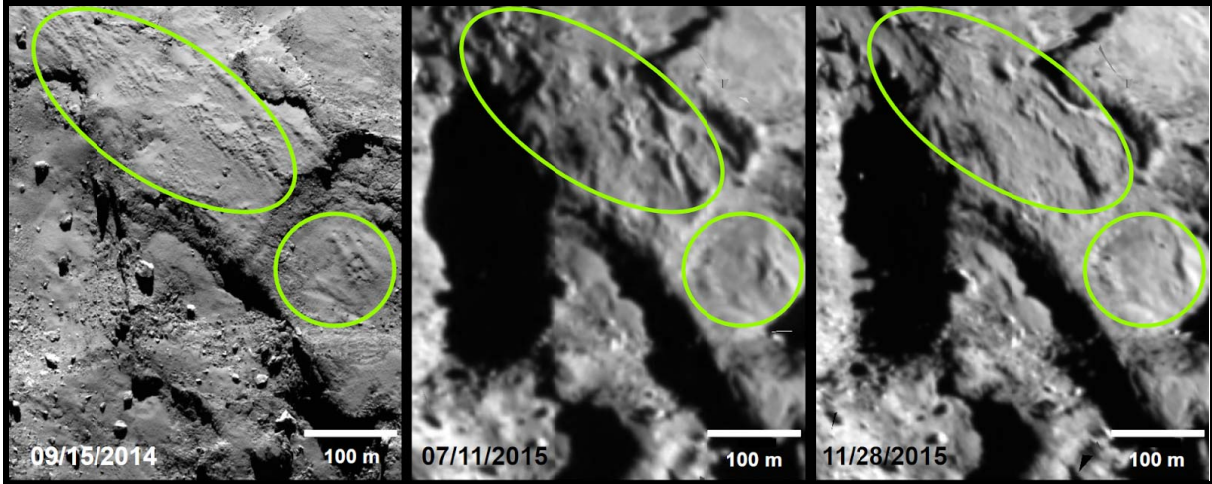
298

299

300

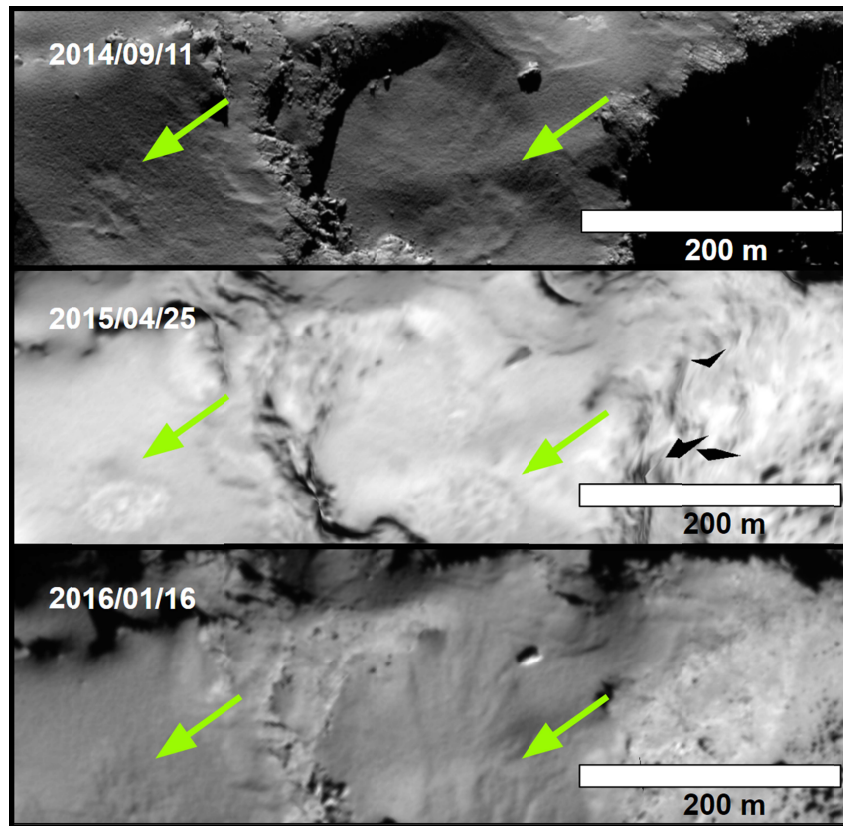
301

Figure 2. a) Co-registered images of Hapi 1 showing arcuate scarp fronts migrating (green arrows) between March 5 and April 25, 2015. b) One boulder exposure circled in green and one boulder burial circled in red, seen in Imhotep 1. c) One boulder sourced from an unknown location migrating into Hapi 1, with notable depressions nearby suggesting it bounced twice.



302
303
304

Figure 3. Co-registered images showing migrating sediment plains in Maftet.



305
306

Figure 4. Co-registered images showing evolving honeycomb structures in Seth 1.

308 We searched for and located many evolving honeycomb features throughout the mission,
309 however our image processing sometimes limited our ability to clearly discern such detailed
310 changes in surface expression. In the case of the depressions on the Ash/Seth border, as well as
311 honeycombs in Serqet, this led to a later detection date in our dataset (~1 month). However, we
312 did often detect the large-scale migrations of plains and crests within smooth terrains, as
313 described above within Ma'at 4, and which we also identified in Seth 1 (January 23, 2015), Seth
314 2 (December 12, 2014) and Hapi 1 (February 14, 2015).

315 We also discovered the first clear evidence of deposition of new smooth terrain materials
316 in Hatmehit, Ma'at 4, Babi 2, Aten 1 and Aten 2 (Figure 4) In February of 2015, regions which
317 are located generally south of the initial erosion activity dominated by Hapi 2 and Hapi 3. We
318 identified isolated instances of boulder and nucleus burials within Babi 2 and Hatmehit on
319 February 19 and February 20, 2015, respectively. The most significant and obvious deposition
320 occurred in Ma'at 4 on the comet's small lobe. In this region, the newly deposited material
321 covered at least 11 large boulders and numerous nucleus outcrops that span the width of the
322 entire sub-region by February 21, 2015. This early deposition marked the beginning of a
323 widespread deposition event which continued in Ma'at 4 and in neighboring regions of Ma'at for
324 several months. Notably, this depositional event over a significant portion of the small lobe
325 coincided precisely with erosional activity in the Hapi 2 region. Hapi 2 is proximal to Ma'at 3
326 and 4, lying just to the north in the deep gravitational low of the neck, perhaps indicating a causal
327 relationship.

328 3.1.3 Pre-Perihelion 3

329 During the next epoch, Pre-Perihelion 3 (March–May, 2015), erosional activity continued
330 to expand southward, including within the low and mid-latitudinal regions of Ash 1, Ma'at 4, and
331 Babi 1. We observed numerous migrating scarps within a highly localized, low latitude area of
332 Ash 1 on April 22 and May 16, 2015. Each scarp appeared to expand radially in an eastward
333 direction, and emanated from the base of a local cliff. We detected polygonal scarps migrating
334 within Babi 1, an internal sub-region of Babi (Fig. 1), from March 14–May 10, 2015. We first
335 saw scarps appear on terraces proximal to the neck in March, followed by the expansion of these
336 scarps and the formation of a new polygonal scarp in a northern terrace of the region by April 19,
337 2015. We also identified a scarp expanding in the southernmost active terrace of Babi 1 by May
338 10, 2015. Hu et al. (2017) also recorded two small scarps migrating in Ma'at 3 by March 28,
339 2015 which exposed part of the underlying nucleus.

340 We observed the continued migration of 10–100 meter scale scarps within Hapi 1, 2, and
341 3 throughout March–May (Birch et al., 2019; El-Maarry et al., 2017; El-Maarry et al., 2019), as
342 many more irregular scarp fronts formed within the three regions. Although Birch et al. (2019)
343 recorded the last day of scarp migration in Hapi 1 to be April 22, 2015, we detected activity up to
344 one month later on May 23, 2015. During the sequence of scarp activity within the neck, we
345 observed the destruction of the ripples by radially expanding scarps within Hapi 1. These scarps
346 first traveled through the region on April 25, 2015, consistent with the observations of El-Maarry
347 et al. (2017; 2019). Scarp migration began in Seth 1 and Seth 2 by March 5, 2015, and continued
348 into April, 2015, coinciding with the redistribution of sediment in these regions. We found
349 further evidence of erosion by the exposures of four boulders within Hapi 1, and three boulders
350 within Seth 1 on April 25, 2015. Additionally, we observed the exposure of the underlying
351 nucleus in Ma'at 4 and sediment slumping in Ash 1, both by May 16, 2015.

352 Honeycombs matured within Serqet, Ma'at 3, and Seth 1 (indicated by an obvious
353 increase in surface roughness) on March 5, March 28, and April 25, 2015, respectively. Hu et al.
354 (2017) also recorded honeycombs evolving in Babi 2 by late March, 2015. Both El-Maarry et al.
355 (2017; 2019) and Hu et al. (2017) identified maturing honeycombs in Serqet, consistent with our
356 own observations in Ma'at 3, as well as those of Shi et al. (2016). Barrucci et al. (2016) and
357 Deshapriya et al. (2016) also described the evolution of one bright patch in Khonsu, which
358 persisted from March 10 to May 22, 2015. These observations indicate that the magnitude and

359 spatial coverage of erosional activity expanded greatly southward as 67P approached equinox in
360 March, 2015.

361 Deposition also greatly expanded during this period. We identified various combinations
362 of nucleus and boulder burials in Serqet and Maftet by March 5, 2015, in Hapi 1 Hapi 2, Ash 1,
363 Ash 3 and Ma'at 4 by April, 2015, and within Seth 1, Serqet, Ma'at 2, Ma'at 3, Ma'at 4, and
364 Imhotep 1 by May, 2015. We detected at least 56 instances of boulder or nucleus burials from
365 March–May, 2015, as well as the burial of a small circular depression in Serqet (May 10, 2015).
366 Erosion and deposition appeared to be occurring simultaneously in several regions during this
367 epoch. This pattern suggests that either (1) local sediment fallback from smooth terrain erosion
368 was working in tandem with the generation of new sediment in the southern hemisphere to
369 reshape the north, and/or (2) transport distances of sediment within smooth terrains occurred
370 over short, sub-kilometer distances.

371 3.2 Near-Perihelion Activity

372 3.2.1 Near-Perihelion 1

373 As the comet approached perihelion, significant gaps in data arose due to Rosetta's
374 orbital configuration. During Near-Perihelion 1 (June–August, 2015), primarily only low
375 latitudinal external (i.e., non-neck or Hathor-facing) regions were analyzed. Hapi 1 and Seth 1
376 were the only internal regions with favorable viewing conditions at this time. In Hapi 1, the
377 earlier group of migrating scarps continued, with two larger scarps approaching and merging
378 with one another between June 27, and July 19, 2015. A ~250 m wide scarp progressed away
379 from the rotation axis, and a scarp shaped like a shepherd's crook unfurled and expanded through
380 the initial location of the aeolian ripples. The two scarp fronts merged on July 19, 2015.
381 Interestingly, we detected the aeolian ripples re-forming at least two distinct crests inside the
382 curved shepherd's crook-shaped scarp, on July 11, 2015 (Fig. S2), several months prior to
383 observations by El-Maarry et al. (2017; 2019). One week after the initial ripple re-formation, a
384 third visible crest formed inside the shepherd's crook-shaped scarp, although the crest positions
385 did not reach their final location until the next epoch. This suggests that these crests (or the
386 intervening relative "anti-crests") have a preference for this location on 67P, perhaps analogous
387 to the pit chains on Phobos (Hortsmann & Melosh, 1989). One isolated scarp formed in Seth 1, on
388 June 17, 2015, but no further activity was visible in the region.

389 We detected varying degrees of erosion in the external regions Ash 4, Hatmehit, Anubis,
390 and Imhotep 1. The most notable activity in Near-Perihelion 1 occurred in Imhotep 1, which
391 includes the primary basin on the large lobe, as well as the western and southwestern alcoves.
392 Within the primary basin and the western alcove, we observed numerous scarp fronts migrating
393 tens to hundreds of meters over the duration of the epoch, specifically on June 5, June 27, July
394 11, July 26, August 1, August 9, and August 23, 2015, consistent with the observations of
395 Groussin et al. (2015) through July 2015. Jindal et al. (2022), recorded the onset of scarp
396 migrations in Imhotep 1 two days prior to our observations, on June 3, and measured an average
397 rate of migration between June 3 and June 27 to be ~23 cm/hr, with migration rates varying
398 between scarps. As the comet drew closer to perihelion (August 13, 2015), scarp activity trended
399 southward, following the subsolar latitude (Jindal et al., 2022). This included the formation of a
400 curvilinear scarp in the southwestern alcove of Imhotep 1 on July 26, 2015 which expanded
401 further south on August 1, 2015. This activity marked the onset of scarp formations and
402 migrations that expanded across the entire Imhotep 1 basin for a brief, but extremely dynamic six

403 month window of time. Barrucci et al. (2016) also recorded the presence of a short-lived bright
404 patch on the eastern periphery of Imhotep 1, coinciding precisely with the onset of the region's
405 scarp activity. The patch persisted from June 5–27, 2015, waning from a diameter of 36–57
406 meters. Barrucci et al. (2016) also noted that bright patch production peaked during this epoch,
407 approximately at perihelion, lending credence to their erosional origins.

408 We identified a scarp front expanding within the pre-existing scarp in Anubis' northern
409 region from July 11–August 1, 2015, and a boulder migrating within an area of coarser sediment
410 farther north on July 26, 2015. We detected two scarps which formed In Ash 4, located north of
411 Imhotep 1 on the face of the large lobe, on June 13, and July 18, 2015, emanating from a
412 western cliff at the edge of the basin. The scarps then migrated eastward and merged on August
413 9, 2015. While we did not observe scarp migrations in Hatmehit, we did see one boulder migrate
414 ~10 m on July 7, 2015, and a patch of plains in the west migrating from June 27–July 7, 2015.
415 Interpreted together, these processes are consistent with local erosion. Plains migrated in several
416 regions across the northern hemisphere, including Serqet (June 25, July 4, 2015), Ash 1 (July 1,
417 2015), Maftet (July 11, 2015), Hapi 1 (July 11, July 25, 2015), and Ash 4 (July 18, August 9,
418 2015). We also found plains migrating in Maftet, which substantially remodeled the distribution
419 of its smooth materials well into Pre-Perihelion 2, though we lack the high-resolution data
420 necessary to precisely determine the end date of this surface activity. On July 11, 2015, one
421 honeycomb feature located amongst Maftet's migrating plains began to change shape slightly as
422 the smooth terrains were locally re-distributed, although it is unclear if the feature's surface
423 roughness visibly changed on this date.

424 Another notable erosional event during this period occurred in Seth 2. A cliff previously
425 referred to as 'Aswan' (Pajola et al., 2016) collapsed at the edge of Seth 2's large, flat terrace
426 (Pajola et al., 2017; El-Maarry et al., 2019). The collapse was first identified on July 15, 2015
427 and created talus deposits which landed on a sediment-covered plateau at a lower elevation,
428 within Hapi 2. Pajola et al. (2017) measured boulders ≥ 1.5 m before and after the cliff collapse to
429 have increased from ~12,000 to ~18,000.

430 The only observable deposition that occurred in this time period was detected in Imhotep
431 1. A meter-scale boulder was buried within the primary Imhotep basin on July 26, 2015. While
432 we did not use the burial of scarps to detect deposition, Jindal et al. (2022) detected the burial of
433 one scarp on July 11, 2015, three scarps on July 26, 2015, a pit on July 31, 2015 and one final
434 scarp on August 6, 2015, indicating that deposition was still occurring during the peak of 67P's
435 erosional activity. This conclusion is particularly supported by images from the weeks after
436 perihelion (23 August–4 September, 2015), as actively migrating scarps were buried by fresh
437 deposition (Jindal et al., 2022). This likely indicates a point at which net local deposition
438 outpaced local erosion in the Imhotep 1 basin. Some of these freshly-deposited smooth terrains
439 may also represent grains that could not escape 67P after being ejected by nearby scarp
440 migration activity.

441 3.2.2 Near-Perihelion 2

442 Resolution decreases further during Near-Perihelion 2 (September–November 2015),
443 with only about half of the regions sufficiently imaged for analyses. Even with such limited
444 information, we see extensive changes to 67P's smooth terrains. Scarps continued to migrate
445 within Imhotep 1, first appearing only in the southern portion of the region on September 2,
446 2015, then expanding again into the northern hemisphere on October 26 and November 21, 2015.
447 A ~100 meter scale scarp migrated south between September 2 and November 21, 2015,

448 exposing a meter scale boulder in the process. We observed no further scarp migration in
449 Imhotep 1 after November 28, 2015, although Jindal et al. (2022) documented the migration of
450 one final scarp in December, 2015. We did identify a migration of the northern, pre-existing
451 scarp front in Anubis on September 15, 2015. By November 28, 2015 both the northern and
452 southern hemispheric scarp fronts remaining in Anubis from 67P's previous perihelion approach
453 migrated. These two scarp migrations were described by El-Maarry et al. (2017; 2019), although
454 they detected these changes in June, 2016. Several smaller scarp fronts within and around these
455 two larger features also migrated by November 28, 2015, indicating widespread erosion across
456 the region. These observations are all coincident with the location of the subsolar latitude.

457 We identified additional evidence of erosion in Aten 1, where four boulders migrated by
458 November 28, 2015, and in Maftet, with sediment continuing to redistribute, exposing one
459 boulder and causing two others to migrate. This local redistribution began in July, 2015, with
460 new crest positions observable as late as February, 2016. During this redistribution process, a
461 ~50 meter long pit formed in the southern area of Maftet on November 23, 2015. We also
462 discovered plains migrating within Anubis (September 15, 2015), Hatmehit (November 7, 2015),
463 Ma'at 4 (November 12, 2015), and Imhotep 2 (November 21, 2015). The most drastic of these
464 changes occurred in Imhotep 2 and Maftet, although our resolution limits us from observing
465 whether the plains within Maftet evolved as rapidly or over longer periods as Imhotep 2.
466 Interestingly, in Anubis the freshly liberated sediment from the erosion described above appears
467 to have redistributed within the same region, burying at least one boulder by November 28, 2015.
468 Similarly, material lofted from within Imhotep 1 appears to have landed southeast in Imhotep 2,
469 burying a small boulder in the western plains on November 21, 2015.

470 We found no further evidence of deposition during this epoch, however Jindal et al.
471 (2022) did observe local deposition in Imhotep 1 by tracking disappearing scarp fronts, noting an
472 interesting change in activity during the weeks following perihelion. They tracked the partial and
473 complete burial of 6 scarps, even as some scarps continued to migrate. This suggests that while
474 deposition and erosion were happening in Imhotep 1 simultaneously, the rate of local deposition
475 across the primary basin began to overcome the rate of local erosion by about November 29,
476 2015 (Jindal et al., 2022).

477 3.3 Post-Perihelion Activity

478 3.3.1 Post-Perihelion 1

479 By Post-Perihelion 1 (December, 2015–February, 2016), Rosetta returned to its lower
480 altitude orbits, which improved resolution sufficiently to view much of the comet surface in
481 detail once again and observe any changes that took place throughout perihelion. The most
482 evident erosion first detected during this period occurred on the small lobe, particularly in Ma'at
483 1, Ma'at 2, and Ma'at 3 from December, 2015 to February, 2016. In addition, we observed
484 several boulder migrations and the formation of quasi-circular, ~5 meter diameter pits in Ma'at 2
485 on January 17, and February 27, 2016. We do not interpret these pits to be scarps because they
486 did not migrate or expand after their initial formation. Similar features formed within Ash 1
487 during Post-Perihelion 2 (described below). Significant erosion also occurred in regions
488 neighboring Ma'at by Post-Perihelion 2. We detected three boulder exposures and three boulder
489 migrations west of Ma'at 1, in Nut by December 20, 2015. As resolution increased further, we
490 observed two more boulder migrations, and 22 boulder exposures, generally in the northern half
491 of the region, on February 27, 2016. Further to the west, in Maftet, the only direct evidence of

492 local erosion came from one boulder migration, which we detected on January 23, 2016. On the
493 face of the small lobe, we identified only limited scarp activity within Hatmehit, where one
494 linear scarp and one curvilinear scarp both expanded southward on December 17, 2015. Five
495 boulders were also exposed across the western half of the region by February 27, 2016.

496 We only observed evidence of erosion in isolated regions on the large lobe during Post-
497 Perihelion 1. The dynamic activity of Imhotep 1 occurring closer to perihelion did not persist.
498 We observed the exposure of circular pits from beneath a sedimentary cover in the eastern region
499 of Imhotep 1 by February 2016, consistent with El-Maarry et al. (2017; 2019). The most
500 significant erosional changes on the large lobe occurred within Khonsu, located southeast of
501 Imhotep 1 (Fig. 1). Activity within Khonsu began by December 18, 2015, where a boulder ~40
502 m in diameter migrated ~170 m northward, carving a scar into the nucleus (El-Maarry et al.,
503 2017). Vincent et al. (2016) describe two possible outbursts which may have triggered the
504 downslope rolling of this massive boulder on August 1, 2015 (Near-Perihelion 1), and on
505 September 14, 2015 (Near-Perihelion 2), indicating that the boulder could have migrated earlier
506 than either El-Maarry et al. (2017) or our own observations suggest. Four scarps also migrated in
507 a patch of smooth terrains located in the northern portion of Khonsu, exposing three boulders
508 along their paths on December 18, 2015. One boulder in the same area and a second boulder
509 located in the center of Khonsu also migrated on this date. Four more boulders migrated across
510 the region, and another five boulders were exposed by migrating plains by January 23, 2016.

511 Three bright pits formed in a central region of Khonsu's smooth terrains on the same date
512 (Fig. 5). The pits appear to have been pre-existing, sediment-mantled structures that were further
513 excavated. Previous analyses suggested that the fresh layer revealed in this process was rich in
514 both water ice and other refractory materials (Deshapriya et al., 2016), (Fornasier et al., 2015),
515 showing spectral similarities to other erosionally active smooth terrains (Deshapriya et al., 2016;
516 Oklay et al., 2016). The pits waned in overall brightness and area over the rest of the mission,
517 however some excess brightness is still detected on July 30, 2016 (Post-Perihelion 3), the last
518 day they were imaged by the Rosetta spacecraft. It is possible that these pits are analogous to
519 bright spots described by Barucci et al. (2016) and Deshapriya et al. (2016). Deshapriya et al.
520 (2016) described two such bright spots in the Khonsu region. The first (bright spot 2) is located
521 on a "boomerang" shaped feature, and persisted from January 23, to June 24, 2016, while the
522 second (bright spot 3) likely had a much shorter lifetime, as it was only observed once on
523 February 10, 2016. Deshapriya et al. (2016) also correlated the presence of bright spot 2 with an
524 outburst which occurred on August 1, 2015 (Vincent et al., 2016), which may indicate that it
525 persisted for almost one year. Similar to the bright pits, Deshapriya et al. (2016) found that the
526 spectra of the bright spots indicated that they were enriched in water ice.

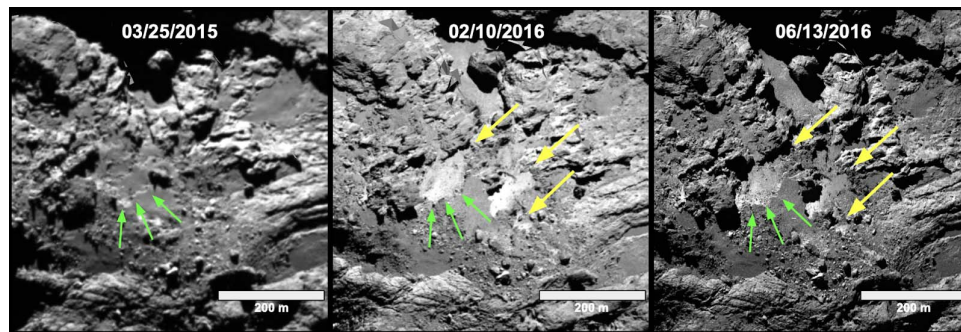
527 To the northwest, eight boulders were exposed by migrating smooth terrains in Imhotep 2
528 on January 23, 2016, after which date we saw no further activity in the region. We detected
529 boulder migrations in Aten 1 on December 2, 2015, and in both Aten 1 and 2 on January 17,
530 2016, after which no further changes in either region occurred. We identified widespread
531 erosional activity southeast of Aten 2, in Ash 4, as six boulders across the region were exposed
532 and one migrated by December 26, 2015. However only one isolated boulder was exposed in
533 Ash 3, north of Aten 2, by December 2, 2015. Similarly, we located one boulder exposure in
534 Babi 2, the external section of Babi west of Aten 1, on December 26, 2015, and the evolution of
535 a pit field in a southeastern alcove of the region by February 27, 2016. We also identified limited
536 erosion within Babi's internal section, Babi 1, although this is one of the few regions in which
537 scarp migrations were still taking place. In Seth 1, another internal region, we detected two

538 boulder migrations. We found slightly more activity in Seth 2, as the boundaries of scarps
 539 bordering the primary terrace migrated and new talus was deposited in two terraces on January
 540 17, 2016. In the neck, Hapi 2 was in polar winter, and was infrequently imaged over this period
 541 of time, preventing our search for surface changes. We did, however, observe active erosion in
 542 Hapi 1 and Hapi 3. Seven boulders were exposed, and one boulder migrated within a
 543 consolidated area on the eastern periphery of Hapi 1, on December 2, 2015. We detected two
 544 more boulder exposures in Hapi 1 on January 9, 2016 with improved image resolution. One
 545 week later, we identified one scarp migration, and two small boulder exposures in Hapi 3.

546 The migration of plains largely coincided with ongoing erosional processes. We observed
 547 migrating smooth terrains in Ash 4 (December 2, December 26, 2015), Ma'at 1 (December 2,
 548 2015), Khonsu (December 18, December 31, 2015, January 23, 2016), Nut (December 20, 2015,
 549 February 27, 2016), Ma'at 2, (January 17, February 27, 2016), Ma'at 3 (January 17, February 27,
 550 2016), Imhotep 2 (January 23, 2016), Maftet (February 10, 2016), Hatmehit (February 27, 2016),
 551 and possibly Babi 2 (December 2, 2015).

552 We also observed deposition across several regions at this time. We detected two boulder
 553 burials in a western strip of Ash 4's smooth terrains on December 2, 2015. We also identified
 554 two boulder burials in Ma'at 1 on the same date, three more within Ma'at 3 by January 17, 2016,
 555 and four boulder burials in Nut by February 27, 2016. Newly deposited material buried an
 556 exposed cliff on the western rim of Imhotep 2 on January 23, 2016, the same area in which a
 557 neighboring boulder was buried during the previous epoch. One boulder was buried within
 558 Khonsu on January 23, 2016, which may be linked to the formation of the spectrally bright pits
 559 nearby. We also observed evidence of deposition in several of these regions by their evolving
 560 honeycomb structures, which decreased in visible surface roughness. These changes occurred
 561 within Ma'at 3, Serqet, and Seth 1 by January 17, 2016. Similar to observations by Jindal et al.
 562 (2022), El-Maarry et al. (2017; 2019) described scarp fronts which previously destroyed Hapi 1's
 563 ripple formation had faded by December 2015. Based on this evidence and our own observations
 564 of newly deposited material in neighboring regions, we interpreted this fading scarp to indicate
 565 local deposition.

566



567

568

569 **Figure 5.** Co-registered images documenting the evolution of bright pits in Khonsu. **Left)** No
 570 bright pits were present on March 25, 2015, although some pre-existing structure that created the
 571 left pit's boundary can be seen (green arrow). The location of future bright pits is covered under
 572 a dust mantle. **Center)** The dust mantle has been eroded to reveal two ~100 meter scale bright
 573 pits, and one 10 meter scale bright pit as seen on February 10, 2016 (green arrows indicate the
 574 left pit's structural boundary, yellow arrows indicate locations of bright spots). **Right)** The bright
 575 pits are still visible on June 13, 2016 (yellow arrows) but they have exhibited an overall
 576 reduction in brightness.

577

3.3.2 Post-Perihelion 2

578 During Post-Perihelion 2 we observed an increase in erosion in the low latitudes of the northern
579 hemisphere as the subsolar point migrated above the equator. We first detected the new exposure
580 of three locations in Ma'at 3 on the small lobe, which may either be boulders or underlying
581 nucleus. Two of these features had been buried during May, 2015. Almost 2 months after this
582 observation, we identified five more boulder exposures in the southernmost portion of Ma'at 1
583 on May 9, 2016. On the large lobe, the most significant erosion during this time occurred in
584 Anubis. While we found two boulder migrations and 41 boulder exposures spanning the length
585 of the region on April 10, 2016, uncertainty in their activity date due to resolution limitations
586 indicates activity could have initiated as early as March 2015. It is likely that these boulder
587 exposures were related to the migration of plains in the center of the Anubis region which we
588 observed on September 15, 2015, when the subsolar point would have been passing through the
589 low latitudes of the southern hemisphere. Also on the large lobe, we detected the possible
590 exposure of 7 boulders in Babi 2 on March 13, 2016, although this observation is questionable
591 due to resolution limitations. We also observed the migration of surrounding plains and the
592 exposure of an outcrop of consolidated nucleus in Babi 2 on April 13, 2016, which had been
593 buried by sediment on February 19, 2015. While we only located one boulder migration in Seth 1
594 on April 28, 2016, we saw less frequent activity in Ash 1. In this region, we detected one boulder
595 exposure, and the formation of 7 quasi-circular pits on April 30, 2016, similar to those that
596 formed within Ma'at 2 during the previous epoch. We identified two more pits forming, although
597 in a different location, within Ash 1 on May 9, 2015. As seen in Ma'at 2, we did not observe
598 these pits growing or migrating after their initial formation, therefore we do not classify them as
599 scarp activity, although they appear to be the result of erosional processing. While we detect no
600 further evidence of sublimation-driven erosion, Deshapriya et al. (2016) documented the
601 formation of a cluster of bright boulders (bright spot 4) on May 7, 2016, which persisted for six
602 weeks after their nominal detection.

603 As described for several other regions above, we observed that simultaneous deposition
604 and erosion occurred in Anubis during Post-Perihelion 2, with much of the redistributed material
605 possibly sourced from the erosion within Anubis, which was exposed to direct solar insolation at
606 the time. Twelve boulders were buried in Anubis by April 10, 2016, primarily within the same
607 region where migrating plains exposed boulders. On the same date, we detected deposition
608 within the neighboring neck region of Hapi 1 that buried two meter-scale boulders, perhaps
609 suggesting that this infalling sediment may have also come from Anubis. El Maarry et al. (2017;
610 2019) recorded the fading or partial burial of the a scarp beneath the ripple formation in June,
611 however we detected the fading of this scarp as early as April 10, 2016, coinciding with the
612 deposition which buried the two boulders described above. Finally, El-Maarry et al. (2017; 2019)
613 also recorded decreased surface roughness in honeycombs within Ma'at 3, although we did not
614 identify this activity until June 5, 2016.

615

3.3.3 Post-Perihelion 3

616 During Post-Perihelion 3, at distances of >3 AU scarp migration effectively ceased,
617 perhaps due to less energy available to sublimate water ice. In fact, all types of evidence for local
618 erosion and deposition decreased dramatically. An outburst was detected in Imhotep 2 on July 3,
619 2016 (Vincent et al., 2016; El-Maarry et al., 2019), although this event did not produce visible
620 changes to nearby smooth terrains. While we did detect boulder exposures, migrations, and
621 burials in several regions, these late observations may have been a result of increased resolution

622 as Rosetta began to orbit closer to 67P's surface. We identified two boulder exposures within a
623 region of migrating plains in Ma'at 2, three boulder exposures and one boulder migration in
624 Ma'at 3, and one sediment slump from smooth materials lying atop a cliff in the northern portion
625 of Ash 3 on June 5, 2016. We observed five boulder exposures within Ash 1 by June 6, 2016,
626 though data coverage and resolution limitations made it difficult to reliably determine when the
627 exposures occurred. We detected 7 boulder exposures in Hapi 1 on June 8, 2016, although
628 similar data limitations suggest that these exposures may have occurred in the previous epoch.
629 Likewise, we located a cluster of 5 boulder exposures in northern Anubis on June 9, 2016 which
630 could have occurred as early as April, 2016. While El-Maarry et al. (2017) showed that the two
631 major pre-existing scarp fronts in Anubis migrated by June, 2016, we show above that these
632 migrations occurred several months earlier, reaching their final positions on November 28, 2015
633 (Near Perihelion 2). Finally, in Khonsu, the visible brightness waned in the two largest ice-rich
634 pits, although all three pits were still relatively bright compared to neighboring materials on June
635 13, 2016. This is the last evidence of erosion we detected in 67P's smooth terrains. Deshapriya et
636 al. (2016) indicated that bright spot 2, also located in the Khonsu region, persisted as late as June
637 24, 2016.

638 As global erosion decreased, we likewise detected less evidence of ongoing deposition.
639 New smooth deposits buried three boulders within Ma'at 3 by June 5, 2016, and one boulder
640 within Hapi 1 by June 8, 2016. We observed no further evidence of deposition after these dates.
641 As Rosetta began orbiting closer to 67P and eventually crash landed on its surface, images of
642 complete to near complete regions of the comet were no longer available, preventing any further
643 analysis of the comet's meter-to decameter scale surface changes.
644

645 **4 Discussion**

646 4.1 Key Takeaways

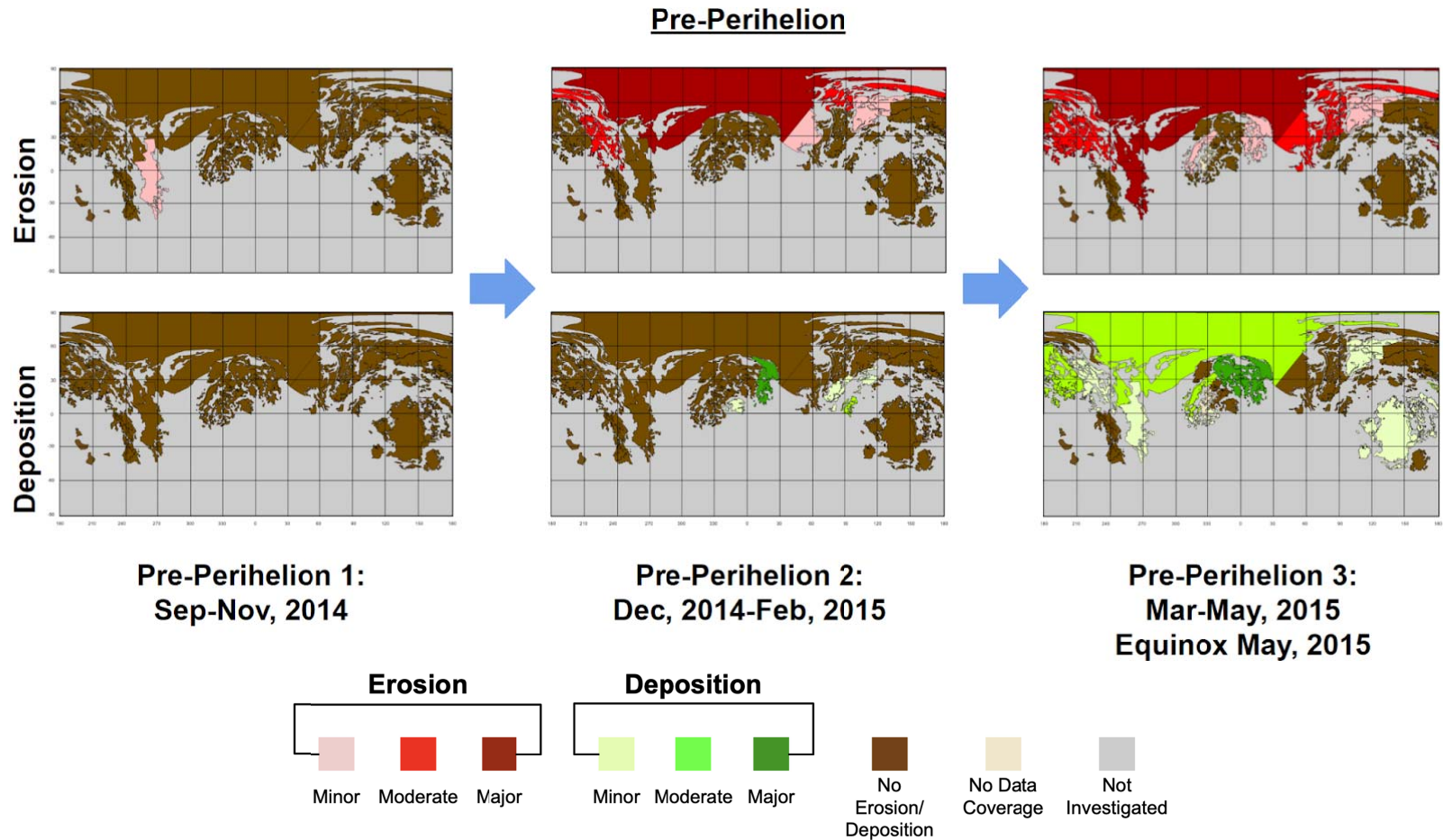
647 Based on the observations described above, we draw four main conclusions.

648 *1) Sediment is intra- and inter-regionally transported.*

649 While previous models suggest that sediment is first sourced by outgassing in the
650 southern hemisphere (Keller et al., 2015), our observations suggest that significant volumes of
651 sediment are also redistributed intra- and inter-regionally after their initial deposition. As the
652 particles deposited within the smooth terrains are likely rich in water ice (Davidsson et al., 2021),
653 we attribute this localized re-distribution to post-emplacement sublimation of ice retained within
654 the sediment itself.

655 Evidence of this redistribution began as early as Pre-Perihelion 2, when the scarps
656 migrating through Hapi 2 began to deposit sediment onto the low- and mid-latitudes of the small
657 lobe, primarily in Ma'at 4 and Hatmehit. This process continued into Pre-Perihelion 3, as
658 escalating scarp activity across Hapi 1, 2 and 3 jettisoned even more material, most of which
659 appeared to deposit on top of the small lobe in regions Ma'at 2–4, and to a lesser extent, in
660 Serqet and Maftet (Fig. 6). Later, in Near-Perihelion 1, the energetic scarp-driven activity in the
661 Imhotep 1 basin intra-regionally redistributed grains, burying a boulder, five scarps, and a pit in
662 the process (Jindal et al., 2022). In Near-Perihelion 2, as scarp migrations continued in Imhotep
663 1, remobilized grains partially or completely buried six scarp fronts in Imhotep 1 and a
664 consolidated cliff in Imhotep 2 (Fig. 7).

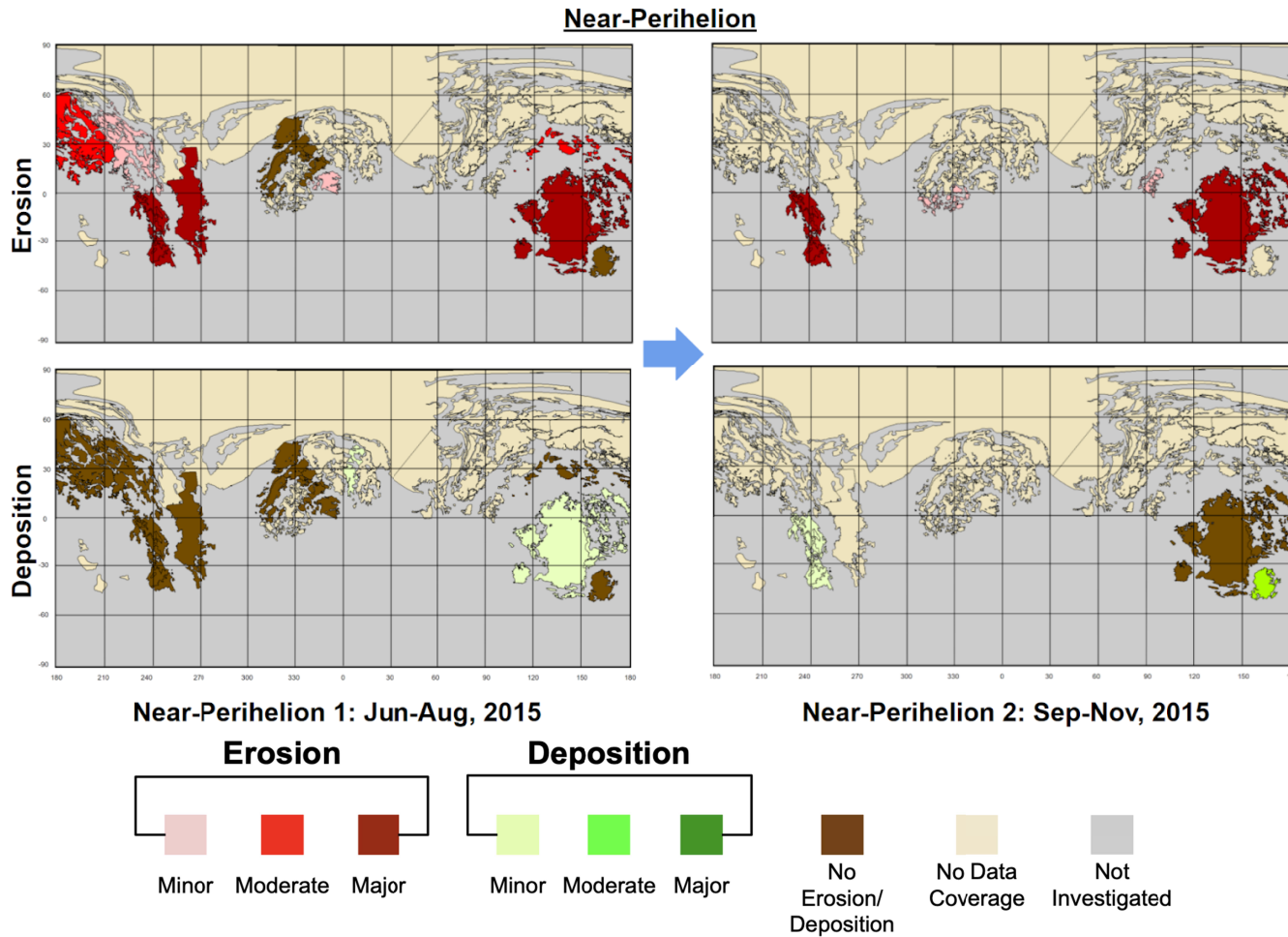
665



666

667

668 **Figure 6.** Equirectangular projections of smooth terrain activity in 67P organized to show the progression of erosion (**top**) and
 669 deposition (**bottom**) across three pre-perihelion time bins. Each column represents one time bin. Maps on the top/bottom indicate
 670 intensity of erosion/deposition. Erosion began in the neck, then also activated in internal regions of the large lobe, followed by lower
 671 latitudes on both lobes. Larger scale deposition occurred during Pre-perihelion 3 in many of the same regions experiencing erosion,
 672 with additional deposition occurring on top of the small lobe in Ma'at 2–4.

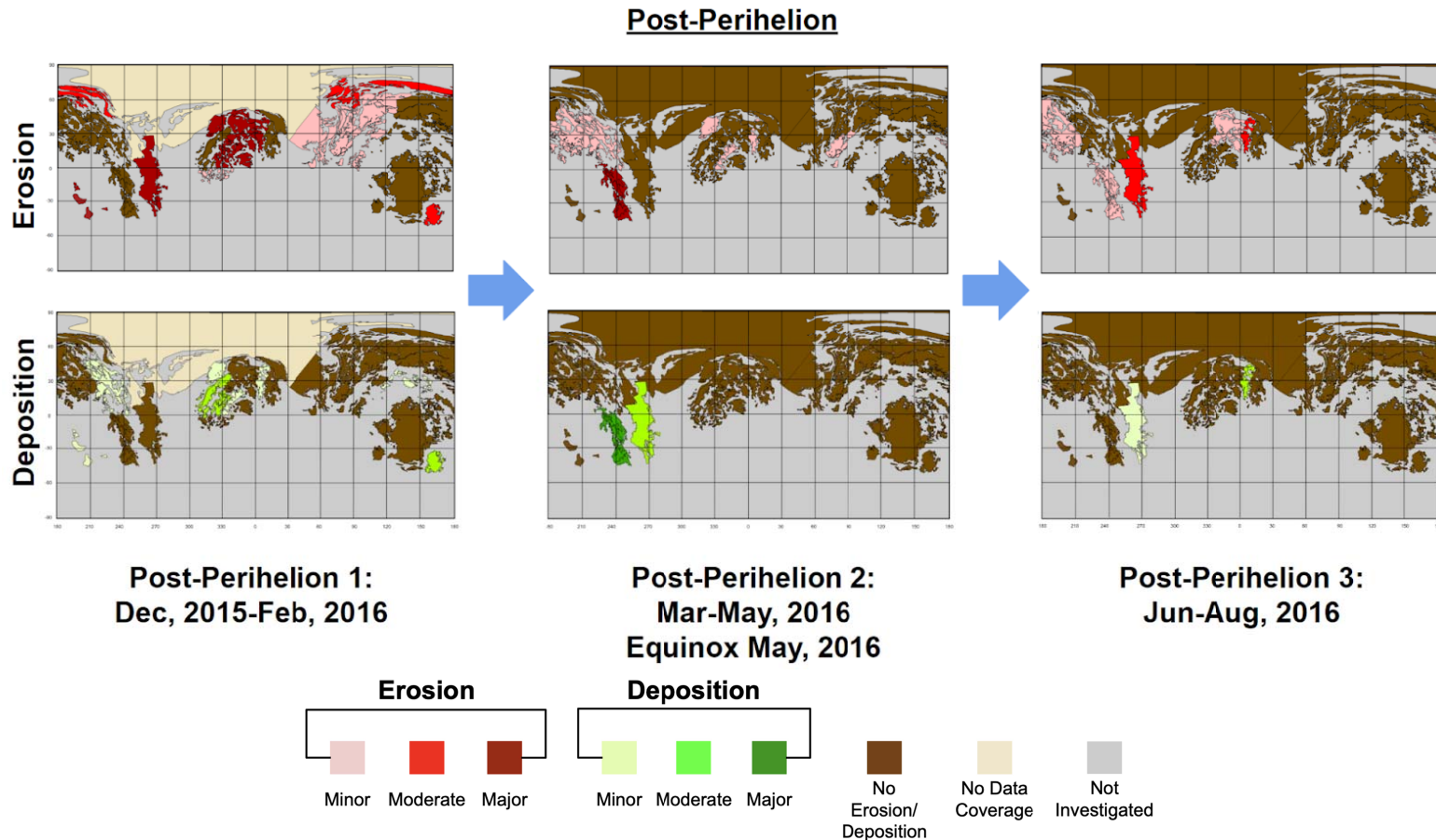


673

674

675 **Figure 7.** Equirectangular projections of smooth terrain activity in 67P organized to show the progression of erosion (**top**) and
 676 deposition (**bottom**) across two time bins near 67P’s perihelion on August 13, 2015. As a result of decreased image resolution, tan-
 677 colored regions were not observable, leaving only the more external regions of the lobe for observation. We observed erosion centered
 678 around the mid to low latitudes over these time bins, with some of the eroded material appearing to locally re-distribute. Material from
 679 Anubis’ scarp migrations appears to fall back into the same region, while sediment lofted from Imhotep 1 appears to deposit both
 680 within the same region, and in the nearby alcove of Imhotep 2.

681



682

683

684 **Figure 8.** Equirectangular projections of smooth terrain activity in 67P organized to show the progression of erosion (**top**) and
 685 deposition (**bottom**) over three time bins occurring after 67P's perihelion passage. As Rosetta returned to lower altitudes, image
 686 resolution improved, revealing the majority of the comet surface for observation by March, 2016. Much of the erosion and deposition
 687 we observed in the northern hemisphere may have occurred closer to perihelion, as a result of the data limitations shown in Fig. 7.
 688 Lower levels of both erosion and deposition continued throughout the remainder of the mission, with spatial trends in the locations of
 689 where material was lofted and re-deposited.

690 Finally, in all Post-Perihelion phases, we observed the redistribution of grains from several sub-
691 regions of Ma'at into Ma'at 3 (Post-Perihelion 1, 2, 3), simultaneous erosion and deposition
692 activity in Khonsu (Post-Perihelion 1) and Anubis (Post-Perihelion 2), and the apparent transport
693 of grains from Anubis to Hapi 1 (Post-Perihelion 2) (Fig. 8).

694 However, a direct link between the possible sources and sinks of material cannot be
695 definitively established. This is largely the result of the sporadic nature over which Rosetta
696 OSIRIS NAC data were acquired, wherein we lack simultaneous observations of both a source
697 and sink region, or any continuous/quasi-continuous imaging capable of resolving a given
698 sediment transport pathway. Instead, we observe two regions eroding and depositing
699 simultaneously and nearby each other (e.g., Hapi 2 and Ma'at 4 in March–May, 2015), and then
700 infer that sediment is transporting between them. Our observations are therefore consistent,
701 though perhaps not diagnostic, with some amount of intra- and inter-regional sediment
702 redistribution, indicating possible sediment transport pathways by which smooth terrains can
703 rearrange on 67P over time.

704

705 *2) Erosion and deposition follow the subsolar latitude, and are strongly influenced by local*
706 *topography.*

707 Observable erosion began in the neck in Hapi 1, spread to the rest of the neck and
708 internal/comet-facing regions, progressed ‘southward’ onto the tops of the comet’s lobes, further
709 south onto the face of either lobe, and finally into the southern hemisphere near perihelion (Fig.
710 6–9). The southward progression of erosional activity is consistent with the migration of the
711 subsolar latitude as 67P approached perihelion (Keller & Kührt, 2020). Before perihelion, El-
712 Maarry et al. (2019) and Hu et al. (2017) observed honeycomb maturation in the low- and mid-
713 latitudes of Ma'at, Nut and Serqet south of our own observations of erosion. We interpret these
714 honeycomb evolutions to be some of the earliest indicators of local erosion. We also observed
715 evidence of local enhancement due to topographic self-heating in Hapi 2, where the cliffs of
716 Hathor and Seth 2 re-radiated onto the neck, sustaining scarp migration events for over six
717 months. Locations of enhanced activity in the neck and within isolated pits in other regions were
718 modeled by Keller et al. (2015) and are consistent with observed activity in Hapi 2, as well as
719 scarp activity observed in pits from the Ash 1 and Seth 1 regions.

720 Depositional activity followed a similar, although less direct trend, broadly beginning in
721 regions near the neck and progressing southward, slightly lagging the subsolar latitude. Within
722 any given region, we also observed heterogeneous deposition of new materials, suggesting that
723 sediment transport pathways are often quite short. If we assume the grains initially deposited are
724 water ice-rich (Davidsson et al., 2021), then these local variations could result from two
725 competing effects. First, a given location may have a limited supply of ice-rich sediment,
726 wherein such regions are distant from a given source region or topographic variations block the
727 delivery of new ice-rich particles — quantified via the “deliverability” index of Davidsson et al.
728 (2021). Equally, sediment may either lack the necessary ice needed to re-mobilize sediment due
729 to prolonged exposure during transport/on the surface, or sediment may be relaunched
730 immediately upon deposition — quantified by the “survivability” described in Davidsson et al.
731 (2021).

732 Topography can therefore both shield a location from receiving new material, but also
733 enhance the local erosion rates of any newly deposited material due to self-heating (Jindal et al.,
734 2022). Given the large topographic variations across the comet, the highly localized nature of
735 erosion and deposition is therefore not surprising. This pattern also suggests a remarkable

736 terrestrial analog, wherein the topographic evolution of a given portion of 67P's smooth terrains
737 is controlled by the capacity for sediment to be transported, and the supply over which it is
738 delivered. Just as a river adjusts its geometry to varying sediment supplies, so too do 67P's
739 smooth terrains.

740

741 *3) Scarp activity is primarily limited to equatorial and internal regions.*

742 As the primary driver of erosion in the smooth terrains (Birch et al., 2019), scarp activity
743 is influenced both by the subsolar latitude and the presence of surrounding topography. On
744 external portions of the nucleus, topographic relief is lower, and the presence/absence of scarps
745 follows the subsolar latitude (Fig. 10). This trend was most apparent in Imhotep 1 during 67P's
746 perihelion approach, where scarps began migrating in the northern portion of Imhotep 1 in June,
747 2015. Progressively more southern scarps appeared and began migrating as the comet
748 approached perihelion, consistent with observations by Jindal et al. (2022). By October, 2015,
749 we once again detected scarp migrations in the northern portion of the basin until all migration in
750 Imhotep 1 stopped between November-December, 2015. As a result of this insolation
751 dependence (both direct and re-radiated from surrounding topography), scarp activity was
752 primarily limited to low- to mid-latitudinal regions mostly bordering the equator (Khonsu,
753 Anubis, Hatmehit, Imhotep 1, Ash 4) as 67P approached perihelion.

754 Meanwhile on internal portions of the comet, the influence of topography becomes
755 especially important. Specifically, any given spot of the surface on internal portions of 67P 'sees'
756 significant fractions of the comet above their local horizon (Birch et al., 2019; Jindal et al.,
757 2022). These surfaces then re-radiate onto the smooth terrain regions, providing a secondary heat
758 source that is sufficient to form scarps. This was the case for Hapi 1, Hapi 2, Hapi 3, Seth 1, Seth
759 2, Babi 1, and Ash 1 (Fig. 10). We also observed examples of re-radiation encouraging scarp
760 formation in the neck and in pits containing smooth terrains in Ash 1 and Seth 1, and Imhotep 1
761 along several topographic boundaries that acted as discontinuities from which several scarps
762 generated (Fig. S1).

763 Other smooth terrains on 67P never showed evidence for scarps. In 67P's current orbital
764 configuration, the mid- to high- latitudes (tops of either lobe) were in polar winter as the comet
765 approached perihelion. The subsolar point passed through the lowest latitudes of these regions
766 while the comet was still at distances of >2.5 AU from the Sun, providing much less total solar
767 insolation to the tops of either lobe compared to the other external regions of the comet. Further,
768 these regions lack significant topographic relief and the secondary energy source they provide.

769 Therefore, as in previous work, we suspect that scarp migration results from the complex
770 interactions between 67P's high relief topography and the local, rapidly changing illumination
771 conditions as 67P approached perihelion. This appears to produce highly localized enhancements
772 in the total amount of energy a given location on the surface receives. Combined with the
773 presence of local re-radiating hot spots like boulders or cliffs within the plains (owing to being
774 more conductive) (Marschall et al., 2017), scarp formation ends up being extremely localized,
775 rather than a simple removal of an upper unconsolidated sedimentary layer (Birch et al., 2019;
776 Jindal et al., 2022). This therefore explains why regions near 67P's north pole, which otherwise
777 receive minimal direct illumination, can still host scarps, while for external regions, only those
778 directly illuminated near perihelion 67P display scarps (Fig. 10).

779

780

781 4) *We observe net zero erosion/deposition on the tops of the lobes, perhaps indicating the*
782 *presence of terminal sinks for airfalling sediment.*

783 A final striking pattern we observe is that over 67P's mid-latitudes (30–60° N), which
784 represent the “tops” of each lobe when viewed edge-on, the surface was largely inactive at
785 Rosetta's NAC image resolution (Fig. 11). Although deposition is inherently difficult to discern
786 in the projected images, and the surface could have gained/lost sediment up to ~50 cm depth
787 without our detection (equal to the best resolution Rosetta obtained before/after perihelion), the
788 absence of any activity stands in stark contrast to the rest of the comet. All other regions
789 exhibited at least minor activity and reorganization of the overlying sedimentary cover, while
790 these regions showed almost zero changes of any kind.

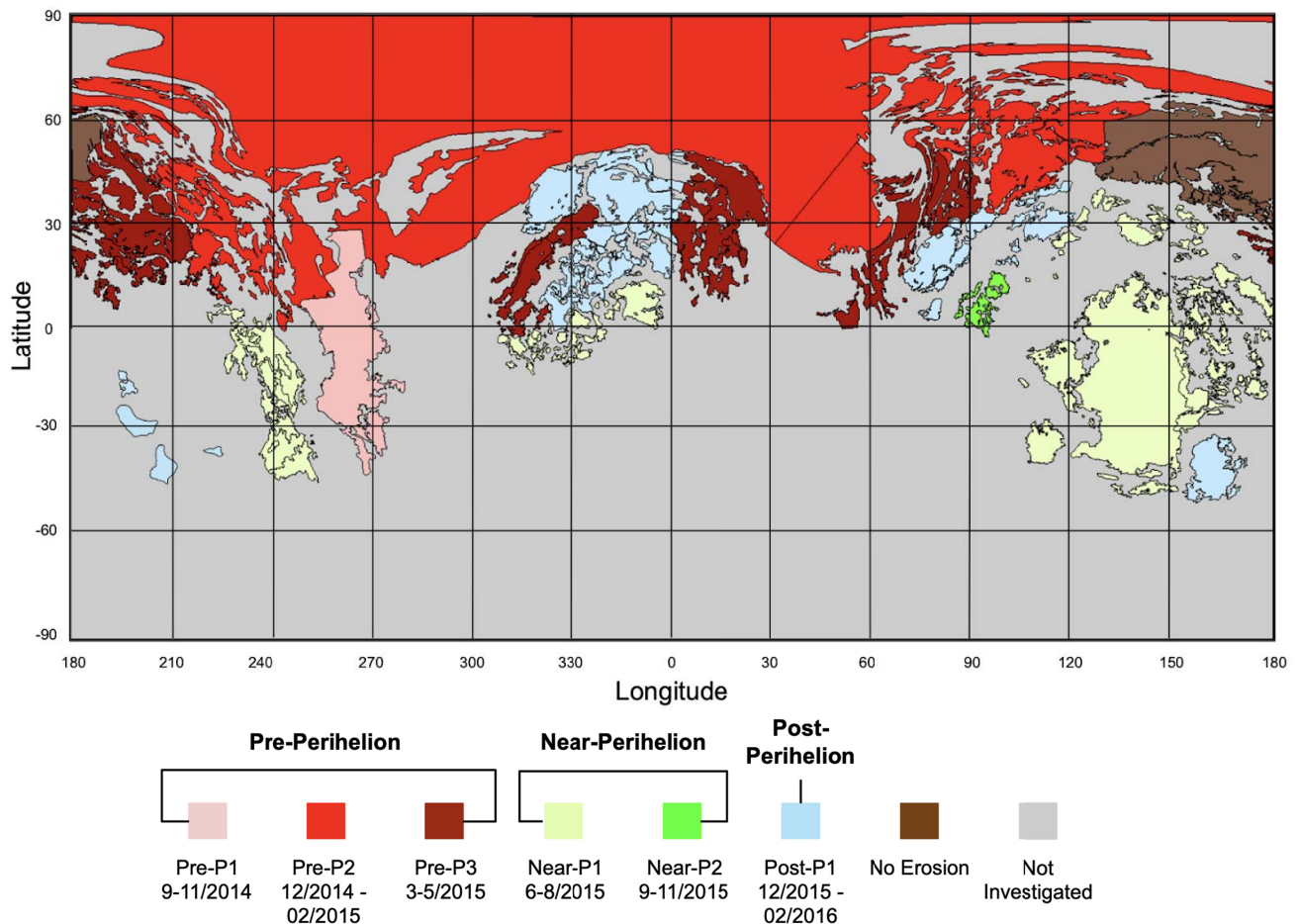
791 The clearest example is Ash 2, where we detected zero deposition or erosion activity of
792 any kind. Also on the large lobe, we observed no activity from 40–60°N in Ash 1, and the mid-
793 latitudinal regions of Babi 1 and Seth 2 (Fig. 11). We likewise identified very limited activity in
794 Ash 3, most of which occurred as slumping of over-steepened mounds of smooth terrains along
795 the margins of overhanging cliffs. While we detected isolated boulder exposures in this region,
796 they were situated on relatively low elevation terraces within the elongated pit of the Aten
797 region. In Ash 3 we likewise identified sediment that coated an outcrop of the underlying nucleus
798 in April, 2015, although the local burial appears to be the result of another gravitational slump of
799 sediment.

800 We also observe limited surface activity from ~40–50°N latitude on the small lobe (Fig.
801 11). Similar to Ash 2 and 3, these latitudes of the small lobe experienced polar night for a
802 prolonged period near perihelion. Although boulders and outcrops of consolidated nucleus were
803 exposed in Ma'at 1–4, this erosion all took place below ~40° N, latitudes that never went into
804 polar winter near perihelion. The remaining section of the top of the small lobe appeared
805 unaltered by local erosion, except for one honeycomb evolution in Ma'at 1 that we interpret to be
806 the result of self-heating from a nearby cliff. While we observed changing honeycomb maturity
807 within the rest of Ma'at due to both erosion and deposition, these features were primarily located
808 between 20–40° N latitude (El-Maarry et al., 2019).

809 The lack of detectable activity in these regions is consistent with previous models. Keller
810 et al., (2015) modeled erosion in these regions and their counterparts on the large lobe and
811 estimated that they should be the least active locations on the comet. Keller et al. (2015) likewise
812 noted that the most active sections of these regions were the sections that slope to the south,
813 consistent with our observations of activity from 20–40° N. Erosion and deposition models from
814 Lai et al. (2016) also suggest that grains from about 0.04–0.08 mm in diameter should have
815 deposited in these regions in January, 2015, but grains from about 0.04–22 mm should have been
816 eroding from the surface in August, 2015. The result of this activity is a net-zero loss of material
817 on the tops of either lobe across all modeled grain sizes (Lai et al., 2016), consistent with our
818 observations.

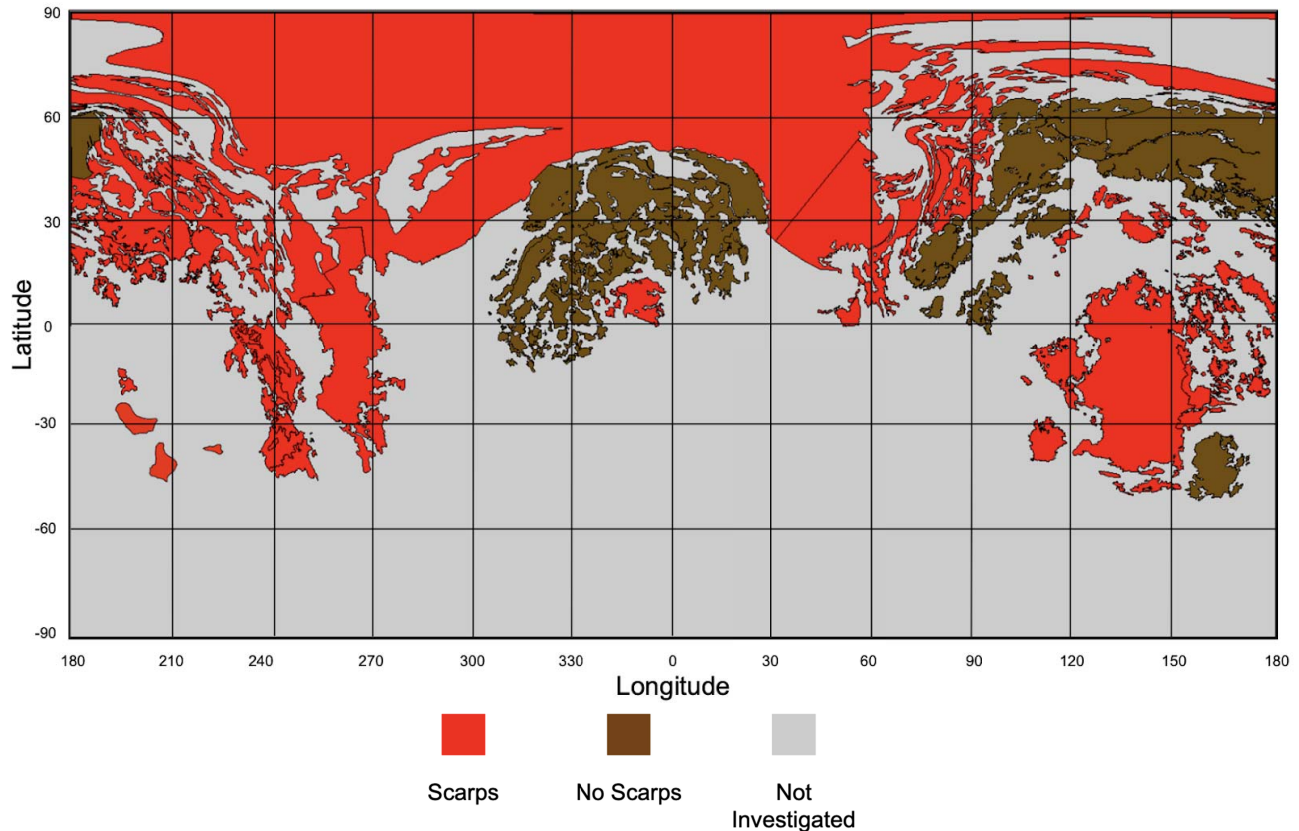
819 Despite the limited observed activity and surface changes, these deposits will likely still
820 evolve thermally. Though the upper centimeters of the surface may be exhausted of their ices,
821 material just below the diurnal skin depth could be especially enriched in volatiles if there is
822 even a small degree of net-deposition to buffer and protect these sediments from sublimating
823 their internal ices. Given how stationary grains on these surfaces may be, sintering may also add
824 a small degree of cohesion. Not only would this armor the surface against subsequent erosion
825 and re-mobilization of deposited grains, but it may also set up subsurface stratigraphy.

826 Specifically, if mixing and granular convection are small, these deposits may have multiple inter-
 827 bedded layers that reflect deposition of new material across multiple orbits.
 828 We therefore interpret these regions as terminal sinks for sediment, where the small amounts of
 829 airfall grains that meet the surface may not be able to subsequently leave, even near perihelion.
 830 Sediment would therefore be transport-limited, and would instead thermally evolve in situ and
 831 more slowly than other smooth terrain deposits over many orbits. Such deposits may therefore
 832 retain larger ice volumes than other smooth terrain deposits on 67P, making them high value
 833 targets for sample return missions. Yet smooth terrains in these regions still bury the underlying
 834 topography. The net-zero activity levels then suggest that these near-polar deposits must
 835 accumulate extremely slowly, or that these deposits accumulated in a different ‘climate’ wherein
 836 67P’s obliquity was more favorable for a more rapid accumulation. Follow-up sediment transport
 837 models should investigate this more rigorously, as well as the potential effects of sintering and
 838 the comparative ice depletion of freshly generated vs. redistributed sediments in order to
 839 understand when these smooth terrains accumulated their sediment and what that implies for
 840 67P’s long-term surface and thermal evolution.
 841



844 **Figure 9.** Equatorial projection showing the onset of local erosion by region, color coded to
 845 show pre-perihelion (shades of red), near-perihelion (shades of green), and post-perihelion
 846 (shades of blue) time bins. Regions in brown show zero evidence of erosion at any point during
 847 the period of our observations, while those in gray were not investigated due to a lack of
 848 observations or smooth terrains.

849



850

851

852 **Figure 10.** Equatorial projection documenting the distribution of scarp activity across 67P by
 853 region. Activity is focused in equatorial regions (~ -30 – 30° latitude), and internal regions which
 854 have increased energy input due to topographic self-heating. Although Ash 1 experienced scarp
 855 activity, all active areas of the region occur below 30° latitude.

856

4.2 Implications for Other Comets

857

858 Of the six resolved comets imaged to date, four were viewed with sufficient resolution to
 859 analyze the comets' surface morphologies. On all four, we observe smooth terrains over some
 860 fraction of their surfaces. While the expression of each of the processes described above may
 861 vary, the sublimation-driven evolutionary processes on 67P have both planetary and cometary
 862 analogs. Mars's scalloped terrains and swiss cheese terrains (Morgenstern et al., 2007; Lefort,
 863 Russell & Thomas 2010), Pluto's pits (Howard et al. 2017), Triton's depressions in its southern
 864 hemisphere terrains (Hansen et al. 2021) and even hollows on Mercury (Thomas, Rothery,
 865 Conway & Anand, 2014) all exhibit striking similarities to scarp fronts observed on 67P, wherein
 866 volatile sublimation liberates refractory grains, driving the back-wasting of scarps. Scarp retreat
 867 is also proposed as a mechanism for the growth of Titan's small lake depressions (Hayes et al.
 868 2016), and occurs across Earth where failure at a cliff base, combined with efficient transport of
 869 the produced sediment, form a characteristic shape (Howard, 1995). Scalloped features have also
 870 been seen on comet 9P/Tempel 1 (Veverka et al., 2013), (Thomas et al., 2013a), providing
 871 evidence of previous scarp migrations on other comets. Additionally, comet 9P/Tempel 1's S2
 872 'flow' boundary recession (Thomas et al., 2013a) closely parallels scarp migrations found on
 67P, where near surface volatile ices sublime and cause the recession of a smooth terrain

873 boundary. While the various expressions of scarp migrations described indicate an influence
874 from various planetary conditions (e.g., gravity, volatile-refractory mixing at the grain scale,
875 presence/absence of an atmosphere, etc.), the underlying physics related to how ice sublimation
876 can initialize the mobilization of grains and result in back-wasting scarp fronts is clearly
877 universal across the solar system.

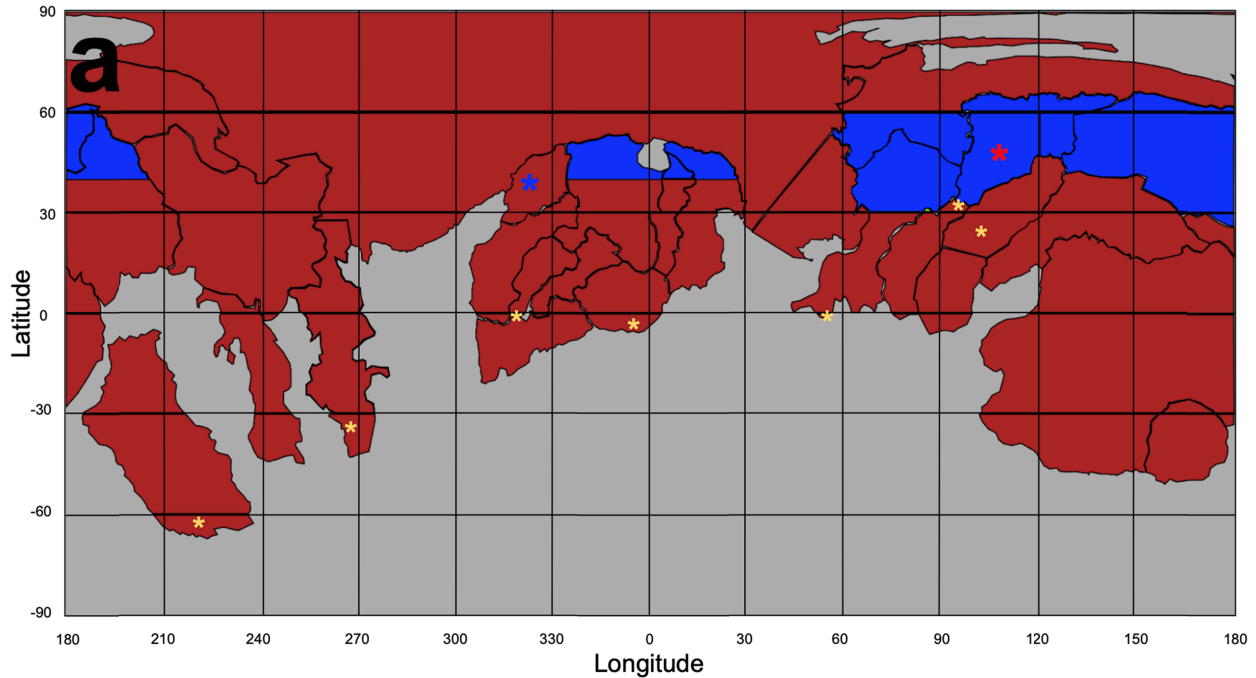
878 We also speculate that the honeycomb features may be analogous to sublimation features
879 on Mars such as brain terrain, which form via differential sublimation processes on thermally
880 fractured surfaces (Hu et al., 2017; Mangold et al., 2003). The small scale and variable
881 expression of honeycombs on 67P could be the result of the highly irregular shape of 67P's
882 surface, or due to highly localized subsurface fractures. These may also represent smaller scale
883 textures that exist in larger plains formations, in which case their presence on other comets
884 would depend largely on local topography, and the surface's propensity to fracture. While we
885 have not detected such features on other comet surfaces, such textures may have occurred at
886 scales that were not resolvable. A more detailed study of these features is warranted, as their
887 formation is unique and remains puzzling (Hu et al., 2017).

888 The process of redistributing smooth terrains via sublimation also likely depends on the
889 physical and compositional parameters of a given comet. Gravity, for example, influences the
890 travel distances of grains. So for comets with equal activity levels, we might expect larger nuclei
891 to have more isolated, thicker deposits of smooth terrains with a larger component of fine grains
892 than smaller comets. Further, larger comets could hold on to more ice-depleted materials since
893 smaller particles rapidly lose their ices (Davidsson et al., 2021). We also expect the obliquity of
894 the comet to influence the distribution of smooth terrains. Objects with a 0° obliquity would
895 likely have smaller smooth terrain deposits centered around one or both of their poles and,
896 excepting regions of gravitational lows, no smooth terrains in the low to mid-latitudes. On the
897 contrary, comets with high obliquity like 67P have larger smooth terrain deposits on the
898 hemisphere that experiences polar winter near perihelion, as re-mobilization at such locations is
899 hampered.

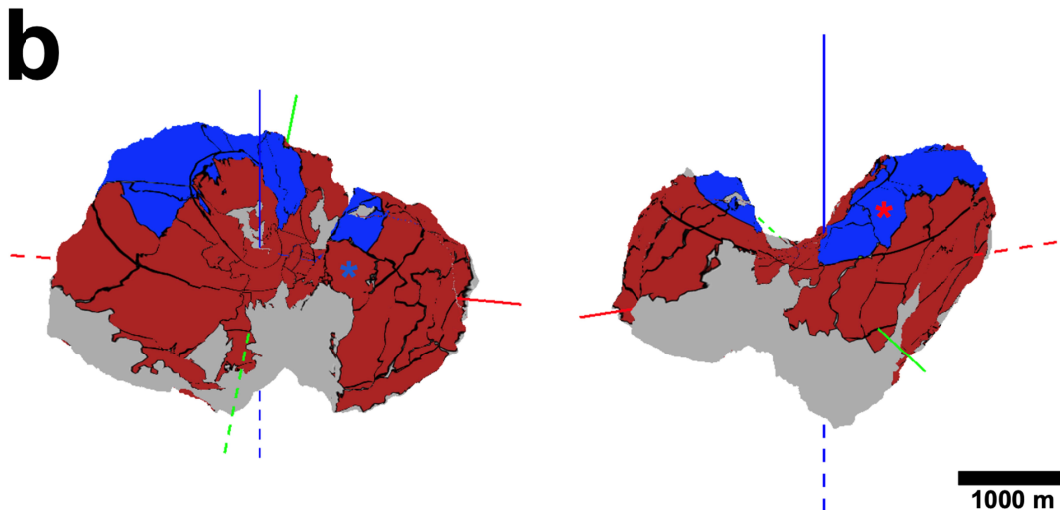
900 If 67P's obliquity were different in the past, the locations where smooth terrains
901 accumulate/erode may have also been different. These expectations are also consistent with
902 observations of two main regions of smooth deposits observed on comet 9P/Tempel 1, which has
903 gravity ~ 1.5 times larger than 67P (Richardson, Melosh, Lisse & Carcich, 2007) and an obliquity
904 of 28° (Sekanina, 1981). On comet 9P, we observe one south polar smooth terrain deposit, and
905 two located in gravitational lows (Thomas et al., 2013a). We also observed smooth terrains
906 within the neck of Hartley 2. With ~ 10 times less gravity than 67P (Thomas et al., 2013b; Sierks
907 et al., 2015; Jia et al., 2017), these potentially larger grains may be more ice-enriched, explaining
908 their observed activity (A'Hearn et al., 2011; Steckloff et al., 2016).

909 Such questions could be also addressed by future landers, orbiters, and flyby missions on
910 this comet, or many others with varying masses and orbital configurations. Because both gravity,
911 obliquity, and timing of perihelion should strongly affect the location, distribution and
912 composition of smooth terrains, they are vital factors to consider when selecting sample sites for
913 future comet sample return missions.

914



915



916

917 **Figure 11. a)** Equirectangular projection showing latitudes with observed erosional or
 918 depositional activity (red), and regions with zero observed activity (blue). Regions are broken
 919 into latitude bins of $\sim 30^\circ$, except for subregions of Ma'at, which are broken into 10° latitude bins
 920 to show inactive areas on the head of the small lobe. Yellow asterisks indicate no activity was
 921 observed in the specific latitude bin, but the area is still interpreted as active overall because it
 922 resides in a broadly active sub-region. The blue asterisk in Ma'at 1 indicates that we observed
 923 very limited and localized erosion which may be connected to topographic influences. We
 924 observed no erosion or deposition within the rest of the region, which may therefore largely
 925 behave as a part of the small lobe's hypothesized terminal sink. The red asterisk indicates limited
 926 activity which appears to be the result of settling of sediment due to gravitational instabilities,
 927 rather than the direct result of sublimation activity—we therefore interpret the region to be a part
 928 of the large lobe's terminal sink extent. **b)** A 3D projection of the regions interpreted as active
 929 (red) or inactive (blue). The Z-axis is shown in blue, the Y-axis in green, and the X-axis in red.
 930 Dashed lines indicate the negative axis direction.

931 **5 Conclusions**

932 We draw four primary conclusions based on our observations:

- 933 1) Sediment is intra- and inter-regionally transported.
- 934 2) Erosion and deposition follow the subsolar latitude, and are strongly influenced by
935 local topography.
- 936 3) Scarp activity is primarily limited to equatorial and internal regions.
- 937 4) We observe net zero erosion/deposition on the tops of the lobes, perhaps indicating
938 the presence of terminal sinks for airfalling sediment.

939 The processes acting on 67P's smooth terrains are driven by the sublimation of volatiles
940 from both the consolidated nucleus and the sediment within the comet's smooth terrain deposits.
941 As the comet approached and passed through perihelion, erosional activity followed the subsolar
942 latitude southward. The primary expression of this erosion is scarp migration, which is mainly
943 limited to low-latitude, external regions and regions where topography provides localized heating
944 due to re-radiation (i.e. neck and lobe-facing regions, pits in Ash 1 and Seth 1). The increase in
945 erosion as 67P approached perihelion led to intra- and inter-regional redistribution of sediment
946 within the smooth terrains. This re-distribution confirms that some volatile ices survive the
947 transport process from the consolidated southern hemisphere to the smooth terrain deposits in the
948 north. To sample recently deposited grains sourced directly from the southern hemisphere,
949 collection sites should be selected from more southern smooth terrains where scarp fading and
950 burial can be tracked as indicators of recent deposition (e.g., Imhotep). External regions between
951 $\sim 30\text{--}60^\circ$ N experience polar winter during perihelion. At these northern extents, near-zero net
952 erosion and deposition occurs. In a slightly net-depositional environment, this may create
953 terminal sinks where any deposited sediment is less able to be removed from the surface in 67P's
954 current orbital configuration. Such terminal sinks represent valuable locations that probe the
955 paleoclimate of 67P and may also represent optimal sample collection sites. On other comets,
956 their mass, obliquity, and timing of perihelion will likely affect the formation and location of
957 terminal sinks, and more generally the distribution and composition of smooth terrains.

958 **Acknowledgments**

959 This research was supported by a Rosetta Data Analysis Program grant
960 #80NSSC19K1307 and by the Heising-Simons Foundation (51 Pegasi b Fellowship to S.B.). We
961 would like to acknowledge Björn Davidsson, who provided helpful comments on earlier versions
962 of this manuscript. We would also like to acknowledge the Principal Investigator of the OSIRIS
963 camera on ESA's Rosetta spacecraft, Holger Sierks, and the ESA Planetary Science Archive for
964 the data used in this study. This research has made use of the scientific software ShapeViewer
965 (<http://www.comet-toolbox.com/>).

966

967

968 **Open Research**

969 All raw images are available on ESA's Archive Image Browser
 970 (<https://imagearchives.esac.esa.int>). ShapeViewer 4.0.0 software is publicly available for
 971 download at www.comet-toolbox.com. ArcMap software is available at
 972 <https://www.esri.com/en-us/arcgis/products/arcgis-for-personal-use/buy> with registration and
 973 fee. All relevant ArcMap projects, shapefiles, layers, and basemaps are available on
 974 <https://hayesresearchgroup.com/data-products/>.

975

976 **References**

- 977 A'Hearn, M. F. et al, (2011), EPOXI at Comet Hartley 2, *Science*, 332(6036), 1396-1400.
 978 <https://doi.org/10.1126/science.1204054>
- 979 A'Hearn, M. F. et al, (2012), Cometary Volatiles and The Origin of Comets, *The Astrophysical*
 980 *Journal*, 758, 29-36. <https://doi.org/10.1088/0004-637X/758/1/29>
- 981 Belton, M. J. S. et al., (2013), The complex spin state of 103P/Hartley 2: Kinematics and
 982 orientation in space. *Icarus*, 222(2), 595-609. <https://doi.org/10.1016/j.icarus.2012.06.037>
- 983 Birch, S. P. D. et al., (2017), Geomorphology of comet 67P/Churyumov-Gerasimenko, *Monthly*
 984 *Notices of the Royal Astronomical Society*, 469(Suppl_2), S50-S67.
 985 <https://doi.org/10.1093/mnras/stx1096>
- 986 Birch, S. P. D. et al., (2019), Migrating Scarps as a Significant Driver for Cometary Surface
 987 Evolution, *Geophysical Research Letters*, 46(22), 12794-12804.
 988 <https://doi.org/10.1029/2019GL083982>
- 989 Brownlee, D. E. et al., (2004), Surface of young Jupiter family comet 81P/Wild 2: View from the
 990 Stardust spacecraft, *Science*, 304(5678), 1764-1769. <https://doi.org/10.1126/science.1097899>
- 991 Davidsson, B. J. R. et al., (2021), Airfall on Comet 67P/Churyumov-Gerasimenko, *Icarus*, 354,
 992 114004. <https://doi.org/10.1016/j.icarus.2020.114004>
- 993 Deshapriya, J. D. P. et al., (2016), Spectrophotometry of the Khonsu region on the comet
 994 67P/Churyumov-Gerasimenko using OSIRIS instrument images, *Monthly Notices of the Royal*
 995 *Astronomical Society*, 462(Suppl 1), S274-S286. <https://doi.org/10.1093/mnras/stw2530>
- 996 El-Maarry, M. R. et al., (2015), Regional surface morphology of comet 67P/Churyumov-
 997 Gerasimenko from Rosetta/OSIRIS images, *Astronomy & Astrophysics*, 583, A26.
<https://doi.org/10.1051/0004-6361/20152573>
- 998 El-Maarry, M. R. et al., (2017), Surface Changes on Comet 67P/Churyumov-Gerasimenko
 999 Suggest a More Active Past, *Science*, 355(6332), 1392-1395.
 1000 <https://doi.org/10.1126/science.aak9384>
- 1001 El-Maarry, M. R. et al., (2019) Surface Morphology of Comets and Associated Evolutionary
 1002 Processes: A Review of Rosetta's Observations of 67P/Churyumov-Gerasimenko, *Space Science*
 1003 *Review*, 215, 36. <https://doi.org/10.1007/s11214-019-0602-1>

- 1004 Fornasier, S. et al., (2015), Spectrophotometric properties of the nucleus of comet
1005 67P/Churyumov-Gerasimenko from the OSIRIS instrument onboard the ROSETTA spacecraft,
1006 *Astronomy & Astrophysics*, 583, A30. <https://doi.org/10.1051/0004-6361/201525901>
- 1007 Hansen, C. J. et al., (2021), Triton: Fascinating Moon, Likely Ocean World, Compelling
1008 Destination!, *Planetary Science Journal*, 2(4), 137-148. <https://doi.org/10.3847/PSJ/abffd2>
- 1009 Hortsman, K. C., Melosh, H. J., (1989) Drainage pits in cohesionless materials: implications for
1010 surface of Phobos. *Journal of Geophysical Research*, 94 (B9), 12433-12441.
1011 <https://doi.org/10.1029/jb094ib09p12433>
- 1012 Howard, A. D. (1995). Simulation modeling and statistical classification of escarpment
1013 planforms. *Geomorphology*, 12(3), 187–214. [https://doi.org/10.1016/0169-555X\(95\)00004-O](https://doi.org/10.1016/0169-555X(95)00004-O)
- 1014 Howard, A. D. et al., (2017). Pluto: Pits and mantles on uplands north and east of Sputnik
1015 Planitia, *Icarus*, 293, 218-230. <https://doi.org/10.1016/j.icarus.2017.02.027>
- 1016 Hu, X. et al., (2017), Seasonal erosion and restoration of the dust cover on comet
1017 67P/Churyumov-Gerasimenko as observed by OSIRIS onboard Rosetta, *Astronomy &*
1018 *Astrophysics*, 604, A114. <https://doi.org/10.1051/0004-6361/20162990>
- 1019 Jia, P., Andreotti, B., and Claudin, P. (2017), Giant ripples on comet 67P/Churyumov-
1020 Gerasimenko sculpted by sunset thermal wind, *PNAS*, 114(10), 2509-2514.
1021 <https://doi.org/10.1073/pnas.1612176114>
- 1022 Jindal, A. S. et al., (2022), Topographically Influenced Evolution of Large-scale Changes in
1023 Comet 67P/Churyumov–Gerasimenko's Imhotep Region, *Planetary Science Journal*, 3,
1024 193. <https://doi.org/10.3847/PSJ/ac7e48>
- 1025 Keller, H. U. et al., (1986) First Halley Multicolour Camera imaging results from Giotto,
1026 *Nature*, 321, 320-326. <https://doi.org/10.1038/321320a0>
- 1027 Keller, H. U. et al., (2007), OSIRIS--The Scientific Camera System Onboard Rosetta, *Space*
1028 *Science Reviews*, 128, 433-506. <https://doi.org/10.1007/s11214-006-9128-4>
- 1029 Keller, H. U. et al., (2015) Insolation, erosion, and morphology of comet 67P/Churyumov-
1030 Gerasimenko, *Astronomy & Astrophysics*, 583, A34.
<https://doi.org/10.1051/0004-6361/201525964>
- 1031 Keller, H. U. et al., (2017), Seasonal mass transfer on the nucleus of comet 67P/Churyumov–
1032 Gerasimenko, *Monthly Notices of the Royal Astronomical Society*, 469(Supple_2), S357–
1033 S371. <https://doi.org/10.1093/mnras/stx1726>
- 1034 Keller, H. U. & Kührt, E. (2020), Cometary Nuclei—From Giotto to Rosetta, *Space Science*
1035 *Reviews*, 216, 14. <https://doi.org/10.1007/s11214-020-0634-6>
- 1036 Lauretta, D. S., et al., (2018), The CAESAR New Frontiers Mission: 2. Sample Science. In *49th*
1037 *Lunar and Planetary Science Conference*, The Woodlands, TX, Contribution Number 2083.
- 1038 Lefort, A., Russell, P. S., & Thomas, N., (2010), Scalloped terrains in the Peneus and
1039 Amphitrites Paterae region of Mars as observed by HiRISE, *Icarus*, 205(1), 259-
1040 268. <https://doi.org/10.1016/j.icarus.2009.06.005>
- 1041 Lisse C. M. et al., (2009), Spitzer Space Telescope Observations of the Nucleus of Comet
1042 103P/Hartley 2, *Publications of the Astronomical Society of the Pacific*, 121(883), 968-
1043 975. <https://doi.org/10.1086/605546>
- 1044 Marschall, R. et al., (2017), Cliffs versus plains: Can ROSINA/COPS and OSIRIS data of comet
1045 67P/Churyumov-Gerasimenko in autumn 2014 constrain inhomogeneous outgassing?,
1046 *Astronomy & Astrophysics*, 605, A112. <https://doi.org/10.1051/0004-6361/201730849>
- 1047 Maquet, L. (2015), The recent dynamical history of comet 67P/Churyumov-Gerasimenko,
1048 *Astronomy & Astrophysics*, 579, A78. <https://doi.org/10.1051/0004-6361/20142541>

- 1049 Mousis, O. et al., (2015), Pits Formation from Volatile Outgassing on 67P/Churyumov-
1050 Gerasimenko, *The Astrophysical Journal Letters*, 814(1), L5. [https://doi.org/10.1088/2041-](https://doi.org/10.1088/2041-8205/814/1/L5)
1051 [8205/814/1/L5](https://doi.org/10.1088/2041-8205/814/1/L5)
- 1052 Oklay, N. et al., (2016), Variegation of comet 67P/Churyumov-Gerasimenko in regions showing
1053 activity, *Astronomy & Astrophysics*, 586, A80. <https://doi.org/10.1051/0004-6361/20152739>
- 1054 Pajola, M. et al., (2016), Aswan site on comet 67P/Churyumov-Gerasimenko: morphology,
1055 boulder evolution, and spectrophotometry. *Astronomy & Astrophysics*. 592, A69.
<https://doi.org/10.1051/0004-6361/20152785>
- 1056 Pajola, M. et al., (2017), The pebbles/boulders size distributions on Sais: *Rosetta's* final landing
1057 site on comet 67P/Churyumov-Gerasimenko, *Monthly Notices of the Royal Astronomical*
1058 *Society*, 469(Suppl_2), S636-S645. <https://doi.org/10.1093/mnras/stx1620>
- 1059 Reinhard, R., (1986), The Giotto Encounter with Comet Halley, *Nature*, 321, 313-318.
1060 <https://doi.org/10.1038/321313a0>
- 1061 Richardson, J. E., Melosh, H. J., Lisse, C.M., & Carcich, B., (2007), A ballistics analysis of the
1062 Deep Impact ejecta plume: Determining Comet Tempel 1's gravity, mass, and density, *Icarus*,
1063 191(2), Supplement, 176-209. <https://doi.org/10.1016/j.icarus.2007.08.033>
- 1064 Sekanina, Z., (1981), Rotation and Precession of Cometary Nuclei, *Annual Review of Earth and*
1065 *Planetary Sciences*, 9, 113-145. <https://doi.org/10.1146/annurev.ea.09.050181.000553>
- 1066 Shi, X., et al., (2016), Sunset jets observed on comet 67P/Churyumov-Gerasimenko sustained by
1067 subsurface thermal lag, *Astronomy & Astrophysics*, 586, A7. [https://doi.org/10.1051/0004-](https://doi.org/10.1051/0004-6361/201527123)
1068 [6361/201527123](https://doi.org/10.1051/0004-6361/201527123)
- 1069 Sierks, H. et al., (2015), On the nucleus structure and activity of comet 67P/Churyumov-
1070 Gerasimenko, *Science*, 347(6220), 1044. <https://doi.org/10.1126/science.aaa1044>
- 1071 Sodorblom, L. A. et al., (2002), Observations of comet 19/Borrelly by the miniature integrated
1072 camera and spectrometer aboard Deep Space 1, *Science*, 296(5570), 1087-1091.
1073 <https://doi.org/10.1126/science.1069527>
- 1074 Squyres, S. W. et al., (2018) The CAESAR New Frontiers Mission: 1. Overview, In *49th Lunar*
1075 *and Planetary Science Conference*, The Woodlands, TX, Contribution Number 2083.
- 1076 Steckloff, J. K. et al., (2016), Rotationally induced surface slope-instabilities and the activation
1077 of CO₂ activity on comet 103P/Hartley 2, *Icarus*, 272, 60-69.
1078 <https://doi.org/10.1016/j.icarus.2016.02.026>
- 1079 Sunshine, J. M., Thomas, N., El-Maarry, M. R., and Farnham, T. L., (2016), Evidence for
1080 Geologic Processes on Comets, *J. Geophys. Res. Planets*, 121(11), 2194-
1081 2210. <https://doi.org/10.1002/2016JE005119>
- 1082 Thomas, N. et al., (2015), The morphological diversity of comet 67P/Churyumov-Gerasimenko,
1083 *Science*, 347(6220), aaa0440. <https://doi.org/10.1126/science.aaa0440>
- 1084 Thomas, N et al., (2015b), Redistribution of particles across the nucleus of comet
1085 67P/Churyumov-Gerasimenko, *Astronomy & Astrophysics*, 583, A17.
1086 <https://doi.org/10.1051/0004-6361/20152609>
- 1087 Thomas, P. C. et al., (2013a), The nucleus of comet 9P/Tempel 1: Shape and geology from two
1088 flybys, *Icarus*, 222(2), 453-466. <https://doi.org/10.1016/j.icarus.2012.02.037>
- 1089 Thomas, P. C. et al., (2013b), Shape, density, and geology of the nucleus of comet 103P/Hartley
1090 2, *Icarus*, 222(2), 550-558. <https://doi.org/10.1016/j.icarus.2012.05.034>
- 1091 Thomas, R. J., Rothery, D. A., Conway, S. J., & Anand, M. (2014), Hollows on Mercury:
1092 Materials and mechanisms involved in their formation, *Icarus*, 229, 221-235.
1093 <https://doi.org/10.1016/j.icarus.2013.11.018>

- 1094 Tsou, P. et al., (2004), Stardust encounters comet 81P//Wild 2, *Journal of Geophysical Research*,
1095 109(E12), S01. <https://doi.org/10.1029/2004JE002317>
- 1096 Veverka, J. et al., (2013), Return to comet Tempel 1: Overview of Stardust NExT results, *Icarus*,
1097 222 (2), 424-435. <https://doi.org/10.1016/j.icarus.2012.03.034>
- 1098 Vincent, J.-B. et al., (2015), Large heterogeneities in comet 67P as revealed by active pits from
1099 sinkhole collapse, *Nature*, 523, 63-66. <https://doi.org/10.1038/nature14564>
- 1100 Vincent, J.-B. et al., (2016), Summer fireworks on comet 67P, *Monthly Notices of the Royal*
1101 *Astronomical Society*, 462(Suppl_1), S184-S194. <https://doi.org/10.1093/mnras/stw2409>
- 1102 Vincent, J.-B. et al. (2018), ShapeViewer, a software for the scientific mapping and
1103 morphological analysis of small bodies, *49th Lunar and Planetary Science Conference*, Abstract
1104 #1281.